

# A printed memtransistor utilizing a hybrid perovskite/organic heterojunction channel

*Chun Ma<sup>†</sup>, Hu Chen<sup>†</sup>, Emre Yengel<sup>†</sup>, Hendrik Faber<sup>†</sup>, Jafar I. Khan<sup>†</sup>, Ming-Chun Tang<sup>†</sup>, Ruipeng Li<sup>‡</sup>, Kalaivanan Loganathan<sup>†</sup>, Yuanbao Lin<sup>†</sup>, Weimin Zhang<sup>†</sup>, Frédéric Laquai<sup>†</sup>, Iain McCulloch<sup>†</sup> & Thomas D. Anthopoulos<sup>†\*</sup>*

<sup>†</sup> King Abdullah University of Science and Technology (KAUST), KAUST Solar Center, Thuwal 23955-6900, Saudi Arabia. E-mail: [thomas.anthopoulos@kaust.edu.sa](mailto:thomas.anthopoulos@kaust.edu.sa)

<sup>‡</sup> National Synchrotron Light Source II, Brookhaven National Laboratory  
Upton, New York 11973, United States

KEYWORDS: Hybrid perovskites; conjugated polymer; memtransistor; heterojunction; neuromorphic device.

## ABSTRACT

Neuromorphic computing has the potential to address the inherent limitations of conventional integrated circuit technology, ranging from perception, pattern recognition to memory and decision-making<sup>1-3</sup>. Despite their low power consumption<sup>4</sup>, traditional two-terminal memristors can perform only a single function while lacking heterosynaptic plasticity.<sup>5</sup> Inspired by unconditioned reflex, multi-terminal memristive transistors (memtransistor) were developed to realize complex functions, such as multi-terminal modulation and heterosynaptic plasticity<sup>6</sup>. Here we combine a hybrid metal halide perovskite with an organic conjugated polymer to form heterojunction transistors that are responsive to both electrical and optical stimuli. We show that the synergistic effects of photo-induced ion migration in the perovskite and electronic transport in the polymer layers, can be exploited to realize memristive functions. The device combines reversible, non-volatile conductance modulation with large switching current ratios, high endurance and long retention times. Using in-situ scanning Kelvin probe microscopy and variable temperature charge transport measurement, we correlate the collective effects of bias- and photo-induced ion migration with the heterosynaptic behaviour observed in this hybrid memtransistor. The hybrid heterojunction channel concept is expected to be applicable to other material combinations making it a promising platform for deployment in innovative neuromorphic devices of the future.

## Introduction

Inspired by the morphology and function of  $10^{14}$  synapses in the mammalian brain, silicon-based asynchronous spiking neural networks (SNNs) have ushered in an era of developing non-volatile resistive switching as memristors for artificial intelligence<sup>7</sup>. However, several attempts to break

through the Von Neumann bottleneck, such as crossbar neural network and field-effect transistors with ionic gates<sup>8,9</sup>, have failed to demonstrate heterosynaptic plasticity and focused primarily on singular electrical input<sup>6</sup>. Recently, researchers utilized different types of materials to realize neuromorphic computing with tunable resistance switching. Yoeri *et al.* demonstrated an electrochemical neuromorphic organic device based on PEDOT:PSS/PEI<sup>10</sup> while Vinod, *et al.* reported multi-terminal memtransistors from transition metal dichalcogenides (TMDs)<sup>6</sup>. They both utilized the nature of ionic charge transfer and electromigration within the active materials. An alternative approach was adopted by Choi *et al.* which demonstrated epitaxial random-access memory (RAM) devices using etched single-crystalline SiGe in which an ionic pathway was engineered to realize localized filamentary conduction<sup>11</sup>. Overall, various strategies related to resistance switching have been developed, and the exploration of one or more materials with complementary functionalities is becoming the key for future developments.

Over the past decade, methylammonium lead halide perovskites (PVKs) have attracted enormous attention for application in photovoltaic, (opto)electronic and photonic devices due to their intriguing physical properties<sup>12</sup>. In addition to their well-known application in photovoltaics<sup>13, 14</sup>, PVKs have been explored for other devices such as photodetectors<sup>15</sup>, light-emitting diodes and transistors<sup>16, 17</sup>, and resistance switching devices<sup>18</sup>. An intriguing effect associated with the prototypical PVK material methylammonium lead triiodide (MAPbI<sub>3</sub>), is the giant switchable photovoltaic effect that results in commonly observed hysteresis in photovoltaic cells<sup>19</sup>. Recent studies have attributed the observed hysteresis to ion migration and the light tunable electron-ion interaction within the halide perovskites<sup>20-22</sup>. This mixed conduction character of PVKs inspired us to construct a novel form of non-Von Neumann memory devices whose functions can be tuned by multiple input stimuli to realize neuromorphic computing.

Herein, we describe the development a hybrid memtransistor based on a solution-processed heterojunction (HJ) consisting of the mixed halides perovskite  $\text{MAPbI}_{3-x}\text{Br}_x$  and the indacenodithiophene–benzothiadiazole copolymer (IDT-BT). The memtransistor operation can be controlled by electrical as well as optical signals due to light-controlled ion migration in the heterojunction channel. The resulting devices show high gate tunability ( $>10^5$ ) with large switching current ratios ( $10^2$ ), high endurance ( $>10^2$  times) and excellent retention ( $10^3$  s). Due to the pronounced photo-induced halide redistribution occurring upon electric field application, the memtransistor exhibit distinct light-enhanced plasticity, making it promising for pattern recognition directly in the optical domain<sup>23</sup>. In-situ scanning Kelvin probe microscopy (SKPM) and temperature dependent charge transport measurements provide unique insights in the kinetics of the electric bias and photo-induced ion migration that underpin device operation. The seamless integration of optical and electric inputs is the first step towards complex neuromorphic learning.

### **Optical and structural properties of the hybrid channel**

We employed the bottom-contact, top-gate (BC-TG) transistor architecture shown in **Figure 1a** to construct the multi-input modurable memtransistors. The mixed halides perovskite (PVK) layer was processed via spin-coating on top of pre-patterned gold (Au) source and drain (S-D) electrodes, followed by spin-coating of the semiconducting polymer IDT-BT. The heterojunction exhibits a smoother surface topography as compared to the pristine PVK layer (**Figure 1b**). **Figure 1c** shows the energy levels band diagram of the IDT-BT/PVK heterojunction, which was constructed using different experimental techniques including, photo-electron spectroscopy (PESA) in air (**Table S1**) and UV-Vis absorption spectroscopy (**Figure S1a,b**). Cross-sectional analysis of the heterojunction channel using SEM suggests the IDT-BT solution penetrates the PVK layer (**Figure S2a-d**). Importantly, the infiltrated IDT-BT solution does not appear to affect

the integrity of the perovskite layer beneath since the UV-Vis absorption features of PVK and IDT-BT remaining identical in the heterojunction (**Figure 1d**). Furthermore, **Figure S3a,b** show the phase images of the pristine PVK film and the heterojunction, which demonstrate the pristine PVK film has more crystal dislocations than the heterojunction. The height histograms in **Figure S3c** shows that the heterojunction has a smoother surface which may benefit carrier transport. X-ray diffraction (XRD) measurements also show no difference on the diffraction patterns associated with the individual materials and particularly with the orthorhombic phase of the PVK layer [i.e. (110), (220) and (330)] following IDT-BT deposition (**Figure S4a**). Similarly, Raman measurements show no change of the fingerprint peaks for IDT-BT upon deposition on PVK (**Figure S4b**).

The formation of type II heterojunction (**Figure 1c**) implies the possibility for charge transfer between the two layers upon optical excitation. To test this hypothesis, we performed steady-state photoluminescence (PL) measurements. PVK exhibits a single photoluminescence (PL) peak at 773 nm, which is assigned to radiative carrier recombination (**Figure 1e**).<sup>24</sup> The PL signal intensity of the pristine IDT-BT is significantly lower than that of PVK. When IDT-BT is deposited on PVK, the PL signal shows a marked quench with respect to the pristine PVK layer. The UV-Vis absorbance and PL spectra of pristine IDT-BT are shown in **Figure S1** for comparison. The combination of excellent light absorbing and photocarrier generation characteristics of  $\text{MAPbI}_{3-x}\text{Br}_x$ <sup>12, 25</sup> combined with the narrow energy difference (0.1 eV) between the PVK valence band maximum (VBM) and the highest occupied molecular orbital (HOMO) of IDT-BT (**Figure 1c**), supports the charge transfer hypothesis. Further confirmation stems from time-resolved PL (TR-PL) measurements, which yield a PL lifetime of 23 ns of the neat PVK tracked at the emission peak (**Figure 1f**). Optical excitation incident to the PVK side of the bilayer

PVK/IDT-BT shows a reduced lifetime of 2.6 ns, whereas exciting incident to the IDT-BT side shows an even shorter lifetime of 1 ns. The PL decay of PVK in the bilayer is most likely attributed to diffusion-limited charge extraction and interfacial charge recombination, which are two competing processes. Since the PL lifetime is faster in the latter case, charge transfer from PVK IDT-BT appears to be more efficient upon excitation from the polymer side. The latter process is corroborated by time-dependent evolution of the PL peaks shown in **Figure S5**.

### Photo-induced carrier transport

The excellent hole transporting character of IDT-BT<sup>26, 27</sup> is expected to facilitate the formation of a hole-transporting channel when deposited atop the PVK layer and form the hybrid bilayer channel. To test this hypothesis we fabricated transistors using the BC-TG architecture shown in **Figure 1a**. As gate dielectric we used the fluoropolymer CYTOP (**Figure S6**.) due to its inert chemical character and solvent orthogonality towards IDT-BT. Transistors based on pristine IDT-BT channel exhibit excellent p-channel character with a maximum mobility of up to 2.1 cm<sup>2</sup>/Vs in agreement with previous reports (**Figure S7**).<sup>26, 27</sup> The field-effect hole mobility ( $\mu$ ) in the channel was calculated in the saturation operating regime using the gradual channel approximation equation:

$$I_{DS} = \mu C_i \frac{W}{2L} (V_G - V_{TH})^2 \quad (1)$$

where,  $I_{DS}$  is the channel current,  $C_i$  is the capacitance of the CYTOP dielectric ( $\epsilon_r = 2.1$  and 900 nm-thick),  $W$  and  $L$  are the width and length of the channel ( $W/L = 1,000/30 \mu m$ ), respectively, and  $V_{TH}$  is the threshold voltage.

Next we fabricated transistors employing the type II PVK/IDT-BT heterojunction channel (**Figure 1a**) and studied their operating characteristics both in the dark and under illumination with

different light intensities up to  $7.2 \text{ mW/cm}^2$ . Optical illumination was delivered using an inorganic light emitting diode (Thorlabs) with electroluminescence emission peak at 632 nm. The obtained data are presented in **Figure S8a**. Evidently, the device maintains its *p*-channel character while exhibits a systematic increase in the off current with increasing illumination intensity. The latter observation indicates an increased carrier concentration in the channel. The latter is attributed to free carrier photogeneration upon illumination.

To gain further insight of the charge transport process, we performed transient photocurrent measurements using a square light pulses of 2.5 kHz ( $53.9 \text{ mW/cm}^2$ ) and a relatively low source-drain voltage ( $V_{\text{DS}}$ ) of 2 V in order to prevent lateral ion migration which may interfere with the measurements (**Figure S8b**). From the photocurrent response in **Figure S8c** we obtain the rise and fall times of  $\approx 28$  and  $\approx 46 \text{ } \mu\text{s}$ , respectively, yielding a total response time of  $\approx 74 \text{ } \mu\text{s}$ . The latter is significantly faster than previously reported data for single-layer perovskite photoconductors which typically fall in second's scale<sup>15, 28</sup>. We attribute this to the improved hole-extraction and transport across the hybrid channel, further highlighting the advantage of the adopted hybrid heterojunction architecture.<sup>27, 29</sup> The photo-switching function remains stable indicating robust operation which is critical for any practical application (**Figure S8d**).

**Figure S9** shows the energy band diagram of the heterojunction channel under different biasing and illumination conditions. Application of  $V_{\text{G}}$  can modulate the resistivity of the channel primarily by altering the conductivity of the IDT-BT layer. That is because IDT-BT exhibits orders of magnitude higher hole mobility than the PVK material and as such dominates the channel conductance upon hole accumulation at the IDT-BT, in good agreement with our experimental observations (i.e. *p*-channel conduction). On the other hand, PVK is a strong photon absorber and highly efficient in generating free carriers upon photoexcitation, effectively acting as light

sensitizer. These key attributes enable the PVK/IDT-BT transistors (**Figure 1a**) to combine electric field-effect with a strong photo-gating effect (**Figure S8a**), making it ideal as multi-stimulus sensing element.

### Photoinduced ion migration

In addition to charge carrier transport, photoinduced ionic conduction is also anticipated to play an important role within the PVK layer<sup>30</sup>, and as such on the overall performance of the ensuing devices. To better understand its effects, we first studied the crystallinity of the PVK layer at the interfaces and in the bulk using the grazing-incidence wide-angle X-ray scattering (GIWAXS) technique. A two-dimensional GIWAXS pattern of the pristine PVK surface with the incident angle of  $0.05^\circ$  is shown in **Figure 2a**. The ring at  $q_r = 10.27 \text{ nm}^{-1}$  is assigned to the (110) face of PVK.<sup>31</sup> The pattern also provides information about the crystallinity of IDT-BT/PVK interface. The diffused ring seen at  $q_r = 9.75 \text{ nm}^{-1}$  (**Figure 2b**) indicates a new phase present at the IDT-BT/PVK interface. A comparison of the azimuthally integrated 1D plots of the surface of PVK w/ and w/o IDT-BT layer is shown in **Figure 2c**. Since, the GIWAXS peak for  $\text{PbI}_2$  is known to be at  $q_r = 9.1 \text{ nm}^{-1}$ ,<sup>32</sup> we ascribe the peak at  $q_r = 9.75 \text{ nm}^{-1}$  to an iodine-rich perovskite phase due to its larger  $d$ -spacing. In contrast, a weaker iodine-rich perovskite phase is found in the bulk as evident from the azimuthally integrated 1D plots of the bulk of PVK/IDT-BT shown in **Figure S10**. These results suggest that the concentration of I within the PVK layer is higher in regions close to the PVK/IDT-BT interface. Since I is known to be highly mobile within the PVK crystal,<sup>21</sup><sup>30</sup> the presence of I-rich PVK phase present at the interface with IDT-BT could serve as an additional ion pathway, further enhancing the mixed ionic-electronic conduction character of the heterojunction channel. In the case of memristor applications, such processes could prove



extremely valuable by enabling improved functionalities including improved current modulation and robust non-volatile behaviour.

To directly probe the ion migration and resulting electrostatic perturbations across the heterojunction channel (**Figure 2d**), we performed *in situ* scanning Kelvin probe force microscopy (SKPFM) measurements (**Figure 2e**). **Figure 2f** shows an SKPFM image obtained prior to the application of any bias. Evidently, no surface potential gradient along the channel exists. To trigger ion migration, a voltage pulse ( $V_{DS} = -20$  V) of 10 s duration was applied followed by a SKPFM scan (**Figure 2g**). Evidently, the surface potential of the channel closer to the drain electrode increased, indicating the existence of localised ions (I). Line profiles taken from **Figure 2g** reveal a potential difference of  $\approx 40$  meV between the source-drain electrodes (**Figure 2h**), due to the change in the local channel resistance. By comparing the channel's surface potential with its topography (**Figure S11**), we identify large potential changes in regions around the grain boundaries. This finding provides experimental evidence of ion segregation occurring mainly at the grain boundaries (interfaces) in the PVK layer in agreement with previous results on electrical properties of perovskite diodes<sup>33</sup>. We note that this is the first direct observation of ion segregation in the periphery of thin the PVK using the SKPFM technique and highlights the potential use of the approach for further fundamental studies.

The effect of ion migration on the Schottky barrier present at the electrodes/PVK interface, was also investigated using temperature-dependent charge transport measurements. Devices were conditioned at  $V_{DS} = -20$  V for 10 s prior to the temperature dependent measurements (**Figure S12**). Using the thermionic emission model for the Schottky-barrier FETs (SB-FETs)<sup>6</sup>, the effective Schottky barrier heights ( $\phi_b$ ) was calculated, yielding values in the range 30-40 meV, in good agreement with the SKPFM measurements in **Figure 2f-h**. Our experimental results

demonstrate the complementarity of the techniques for the study in emerging mixed conductors such as hybrid perovskites.

### Memtransistor operation

**Figure 3a** shows the electrical characteristics of the heterojunction memtransistor, where a bipolar resistive switching behavior is evident. The PVK/IDT-BT memtransistor enters the high-resistance state (HRS) at the beginning of sweep 1 (60 to 40 V). Applying a few seconds of high-voltage conditioning (training), the device gradually turns to low-resistance state (LRS) and maintains the LRS during the rest of sweep 1 (40 to 0 V). The device turns to the HRS abruptly when the polarity of the source-drain voltage ( $V_{DS}$ ) is reversed. The latter indicates that the resistive states relates to the carrier injection at the electrode/PVK interface. To verify this hypothesis, we studied devices with the same architecture but different metal electrodes, namely Au, Ti, and Ag. We find the Ag electrodes to be easily etched by the acidic precursor, while the Ti electrodes to be protected by their native oxide ( $TiO_2$ ). Compared with Au electrodes, transistors with Ti exhibit lower rectification but higher channel conductance (**Figure S13**) due to improved carrier injection.

During sweep 2 (0 to -60 V in **Figure 3a**), the device gradually switches from HRS to LRS, a state which is maintained during sweep 3 (-60 to 0 V). Again, the channel returns to HRS immediately when the polarity of  $V_{DS}$  changes, and the device gradually transits from HRS to LRS during sweep 4 (0 to 60 V). Unlike filamentary resistive switching, our device acts purely as LRS-LRS memtransistor<sup>6</sup>. Importantly, the gate tunability of the channel current is high ( $\approx 10^4$ ) for  $V_G$  in the range from 0 to -80 V (**Figure 3b**). The operating characteristics of the device are dominated by the current on/off ratio of the polymer channel as well as the PVK layer thickness. To this end,

a PVK thickness of  $\approx 180$  nm (**Figure S14**) is found to yield memtransistor with high on/off ratio ( $\approx 10^5$ ) and hole mobility of  $1.67 \text{ cm}^2/\text{Vs}$  (**Figure 3c**).

**Figure 3d** displays 100 consecutive  $I_{\text{DS}}$  vs.  $V_{\text{DS}}$  sweeps measured for an IDT-BT/PVK memtransistor ( $V_{\text{G}} = -10 \text{ V}$ ) in the dark, highlighting the highly stable bipolar switching characteristics of the device. **Figure 3e** shows the endurance characteristics of the same device while being reprogrammed 100 times between LRS and HRS. The  $I_{\text{LRS}}$  increases exponentially during the initial subset of measurement cycles with the  $I_{\text{HRS}}$  remaining below 1 nA (at  $V_{\text{DS}} = -20 \text{ V}$ ). The  $I_{\text{LRS}}$  saturates at  $\approx 10^{-7} \text{ A}$ , accompanied by a slow inverse exponential decay. The retention characteristics of the LRS and HRS evaluated within a period of 2 h in the dark, are shown in **Figure S15** and project a reliable state storage. In **Figure 3f** we plot the current difference ( $I_{\text{LRS}} - I_{\text{HRS}}$ ) and switching ratio ( $I_{\text{LRS}}/I_{\text{HRS}}$ ) between LRS and HRS. Evidently, the aforementioned difference (i.e.  $I_{\text{LRS}} - I_{\text{HRS}}$ ) increases with increasing  $V_{\text{G}}$ , further highlighting the important role of the gate potential. The channel current switching ratio reaches a peak at  $V_{\text{G}} = -10 \text{ V}$ , followed by a monotonic drop at higher  $V_{\text{G}}$ . Importantly, the memristors can be reliably fabricated as evident by the statistical analysis of 64 devices processed during several different runs (**Figure 3g**), making them highly promising for neuromorphic computing applications. The excellent reproducibility is attributed to the separation of the ionic and electronic conduction in the different parts of the channel, making the heterojunction a highly interesting architecture for programmable memtransistor applications.

Based on these observations we propose a mechanism governing the operation of the hybrid memtransistor. The characteristic resistive switching behaviour can be divided into four regions (**Figure S16**), each defined by a certain bias regime. In region **1**, positive poling ( $V_{\text{pol}} > 20 \text{ V}$ ) was applied to drain electrode before measuring the  $I_{\text{DS}}$  at a positive  $V_{\text{DS}} (> 0 \text{ V})$ . It has been previously

shown that the iodine vacancy ( $V_I$ ) is the dominant ion in PVK films due to its lower formation energy and higher mobility<sup>34, 35</sup>. As such, we consider positive ions ( $V_I$ ) to be repelled away from the drain electrode (i.e. lower concentration of  $V_I$ ) leading to  $n$ -type self-doping<sup>19</sup>. The latter will enhance hole injection from Au to PVK due to Schottky barrier height lowering. In region **2**, positive poling remains, however, the  $I_{DS}$  is measured at a negative  $V_{DS}$  ( $< 0$  V). Here, PVK layer remains  $n$ -doped close to the drain terminal, which reduces the  $I_{DS}$  and exhibits rectification behaviour similar to a  $p$ - $n$  junction. In region **3**, the negative poling triggers ion migration with  $V_I$  accumulating close to the drain electrode. The reverse bias changes the character of the bipolar junction from  $p$ - $n$  to the  $n$ - $p$  configuration. As a consequence, the  $I_{DS}$  is suppressed in region **4**.

To verify the role of  $V_i$ , we varied the I concentration within the PVK layer. Since  $V_i$  is more mobile than the Br vacancy<sup>36</sup>, we partially exchanged I with Br. GIWAXS and device measurements show that PVK layers with higher Br concentration exhibit improved crystallinity but suppressed resistive switching (**Figure S17**). On the contrary, PVK devices with higher I content show improved switching behavior but poor field-effect modulation (**Figure S17e-g**). Guided by these results, the stoichiometry of the halide concentration was fixed to the optimal ratio of  $\text{MAPbI}_{2.55}\text{Br}_{0.45}$ .

### Photogated memtransistor operation

Next we studied the influence of light on the electrical characteristics of the memtransistors. Our key hypothesis here is that in addition to the gate field, light should also affect both the charge transport (**Figure S8a**) and ion distribution within the channel due to electron-ion interactions in the PVK layer<sup>22</sup> leading to intriguing device behaviour. The aforementioned electron-ion interaction can be described by the following relation

$$I_I^x + h^{\cdot} \rightleftharpoons I_I^x + V_I^{\cdot} \quad (2)$$

where,  $I_I^x$  is neutral iodine atoms on iodine sites,  $h^{\cdot}$  is positive holes, and  $I_I^x$  stands for interstitial iodine atoms with a neutral effective charge. Increasing the carrier density (holes) is thus expected to result to a higher  $V_i$ . This prediction is in agreement with our experimental observations shown in **Figure 3f** which indicates a higher ion-induced current difference ( $I_{LRS}-I_{HRS}$ ) with increasing  $V_G$ . The data also shows that the concentration of holes ( $h^{\cdot}$ ) transferred from the PVK layer to IDT-BT depends on both  $V_G$  and light leading to a pronounced gate (light)-tunable resistance switching.

Due to the multi-input parameter switching behaviour of the device, we attempted to realize memtransistors that exhibit both electrical and optical plasticity. In its simplest form, such multi-input device could imitate the human visual synapse.<sup>37</sup> In the human visual system the retina plays a key role in light-sensing and visual perception through elaborate electrical and optical signal co-processing (**Figure 4a**). In our attempt to emulate the human retina, we approximated the “retina”-like synapse shown in **Figure 4b**. Here, rods and cones are denoted as a single type light-induced neurotransmitter. The bipolar and horizontal cells in the retina are labelled as “modulator”, which introduces lateral inhibition to the system,<sup>38</sup> while **Figure 4c** shows the electric symbol of the bio-inspired memtransistor.

To test the operation of the bio-inspired memtransistor, voltage input spikes were applied to the drain terminal and the excitatory postsynaptic current (EPSC) was measured at the source terminal (**Figure 4c**). To identify the appropriate potential voltage ( $V_{Pot}$ ) and depression voltage ( $V_{Dep}$ ), pinched hysteresis loops with different  $V_{DS}$  sweep range (from  $\pm 20$  to  $\pm 80$  V) were measured in the dark (**Figure 4d**). Upon application of a maximum-sweep voltage of  $\pm 20$  V, the  $p-n$  doping configuration of the device is retained. When the  $V_{DS}$  sweep-range increases to  $\pm 40$  V,

the  $p$ - $n$  junction configuration changes (see direction of hysteresis in **Figure 4d**). Thus, we set the  $V_{\text{Pot}}$  at the critical value of -20 V.

**Figure 4e** shows the evolution of EPSC as a function of the number of voltage pulses applied at the input at different  $V_G$  (0 to -20 V) measured in the dark. The postsynaptic current increases when applying a  $V_{\text{Pot}}$  and decreases when applying a  $V_{\text{Dep}}$  ( $V_G = -20$  V), demonstrating that synaptic plasticity, long-term potentiation (LTP) and long-term depression (LTD), are accelerated by applying a negative  $V_G$ , corresponding to the consolidation of long-term memory.<sup>39,</sup>  
<sup>40</sup> The behaviour is the result of the aforementioned gate field-induced charge carrier density increase. The definition of LTP and LTD is determined by the retention time. As shown in **Figure 2g** and **Figure S15**, the drifted ions retain their position for over 1 hour demonstrating the non-volatile nature of the process. Thus, we defined the stimulus as long term. In ideal neural system, a linear weight update is preferred. However, a non-linear factor (nonlinearity) may be involved to compensate the influence. We used the platform “+NeuroSim” to assess the nonlinearity in our case, which shows the nonlinearity of LTP is 2.4, and that of LTD is -4.88. Illuminating the device with light (**Figure 4f**) results to EPSC that saturates faster when the  $V_G$  is set to -20 V than when it is set to 0 V, even upon the application of identical input spikes ( $V_{\text{Pot}} = -20$  V,  $t_w = 500$  ms,  $t_i = 200$  ms). The ability to accelerate the modulation of the synaptic weight offer potential to improve the recognizing accuracy.<sup>41</sup> Our hybrid heterojunction memtransistor architecture may also be used to construct logic gates that are capable of processing different types of input signals, further complementing their analogue functions. Such capabilities can potentially be exploited to mimic the unconditioned reflex present in humans and animals.<sup>42</sup> Overall, the proposed memtransistors architecture offers new possibilities in combining different semiconductors whilst simultaneously enabling additional functionalities that may prove valuable in future applications.

## Conclusion

In conclusion, we demonstrated a novel artificial synapsis device architecture by integrating a memristor and a phototransistor using a hybrid organic/perovskite heterostructure channel. The hybrid device is able to respond to both optical and electric signals mimicking certain functions of our visual system. This bio-inspired memtransistor exhibit heterosynaptic plasticity and multi-input modulation on plasticity weight. These capabilities can be potentially further optimized and exploited for different applications including, neuromorphic vision systems, optoelectronic resistive random-access memory (OReRAM) and neuromorphic computing.<sup>37</sup> Most importantly, the bilayer channel architecture proposed and demonstrated here paves the way to further research on electronic materials outside the two aforementioned families which could in turn lead to new exciting discoveries.

## Experimental Section/Methods

*Materials preparation:* Methylammonium Iodide ( $\text{CH}_3\text{NH}_3\text{I}$ , MAI, greatcell solar), Methylammonium Bromide ( $\text{CH}_3\text{NH}_3\text{Br}$ , MABr, greatcell solar) and  $\text{PbI}_2$  (99.99%, trace metals basis, TCI),  $\text{PbBr}_2$  (99.99%, trace metals basis, TCI) for 0.8M  $\text{MAPb}(\text{I}_{1-x}\text{Br}_x)_3$  ( $x=0, 0.15, 1$ ) precursor was stirred in a mixed organic solvent of anhydrous N,N-dimethylformamide (DMF, Sigma-Aldrich) and dimethyl sulfoxide (DMSO, Sigma-Aldrich) in a ratio of  $\text{DMF} : \text{DMSO} = 4 : 1$  at 60 °C for 12 h. IDT-BT polymer was dissolved in chlorobenzene (10 mg/mL) in glovebox and stirred at 60 °C for 5 h. The synthesis details can be found elsewhere.<sup>27</sup>

*Device fabrication:* the transistor is in a top-gate bottom-contact configuration. Au electrodes with a thickness of 40 nm were deposited on glass by thermal evaporator (Angstrom). The length (30  $\mu\text{m}$ ) and width (1 cm) of the device were defined by a shadow mask. Before the deposition of perovskite layer, the substrates were treated in UV-ozone. The perovskite precursor was spin-coated on the pre-treated substrates by a consecutive two-step spin-coating at 2,000 and 5,000

r.p.m for 10 and 20 s, respectively. 10 s before the end of the process, 400  $\mu$ L of chlorobenzene was drop-cast on the spinning substrate (2 cm $\times$  2 cm). The substrates were then annealed at 100  $^{\circ}$ C for 45 min. The IDT-BT solution was spin-coated on the PVK layer at 2000 r.p.m for 60 s followed by an annealing process at 100  $^{\circ}$ C for 5 min in nitrogen. CYTOP was then spin-coated on the bilayer at 2000 r.p.m for 60 s. Finally, Al gate electrodes were deposited by thermal evaporation (Angstrom).

*Characterization:* Electrical characterization of transistors was carried out using a Keysight 2912A Precision Source/Measure Unit (SMU) and a probe station (EVERBEING) in a nitrogen-filled glove box. The optoelectronic characterisation was carried out by measuring the current-voltage characteristics of the fabricated devices in dark environment and under various illumination intensities using light-emitting diodes (LEDs, Thorlabs). Specifically, LEDs with electroluminescence emission peaks at 632 nm were employed. Various illumination intensities were achieved by a T-cube driver (Thorlabs). The actual illumination optical powers were calibrated by a Thorlabs 120UV power sensors prior to the measurement.

*Molecular weight analysis:* Number average ( $M_n$ ) and weight-average ( $M_w$ ) molecular weight were determined by Agilent Technologies 1200 series GPC running in chlorobenzene at 80  $^{\circ}$ C, using two PL mixed B columns in series, and calibrated against narrow polydispersity polystyrene standards. Photo Electron Spectroscopy in Air (PESA): PESA spectra were recorded with a Riken Keiki AC-2 PESA spectrometer with a power setting of 5nW and a power number of 0.2. Samples for PESA were prepared on glass substrates by spin-coating. The ultraviolet-visible (UV-Vis) transmission measurements were performed using a Cary-5000 UV–Vis spectrophotometer (Agilent).

*Optical spectroscopy measurements:* Steady-state photoluminescence spectra were recorded using an excitation wavelength of 633 nm on a commercial spectrofluorometer (Horiba). For TR-PL experiments samples were excited with the Coherent Helios 532 nm nanosecond laser with a pulse width of 0.85 nanoseconds and with a repetition rate of 1 kHz. Typical pulse energies were in the range of several  $\mu$ J. The PL of the samples was collected by an optical telescope (consisting of



two plano-convex lenses), and it was further focused on the slit of a spectrograph (PI Spectra Pro SP2300), and eventually detected with a Streak Camera (Hamamatsu C10910) system with a temporal resolution of 1.4 ps (picosecond). The data was acquired in photon counting mode using the Streak Camera software (HPDTA).

*Atomic force microscope (AFM) analysis:* AFM measurements were carried out with a Dimension Icon (Bruker) in air and in the dark. SKPFM measurement was carried out with a scanning probe microscope (Solver next, NT-MDT), and OSCM-PT probes (Veeco) were used in the SKPFM measurements. A Nova Nano- SEM 630 (FEI) was used to acquire cross-sectional images.

*Grazing-incidence wide-angle X-ray scattering (GIWAXS):* The GIWAXS experiments were conducted at CMS beamline (11BM) on NSLS II, Brookhaven National Lab. The wavelength of the X-ray was 1.17 Å with a bandwidth of 0.7%. The scattering signal was collected by a CCD detector, which was placed 220mm away from the sample with a tilt angle of 19° respect to the X-ray beam. The exposure time was 10s. The data analysis was performed by SciAnalysis.

## FIGURES

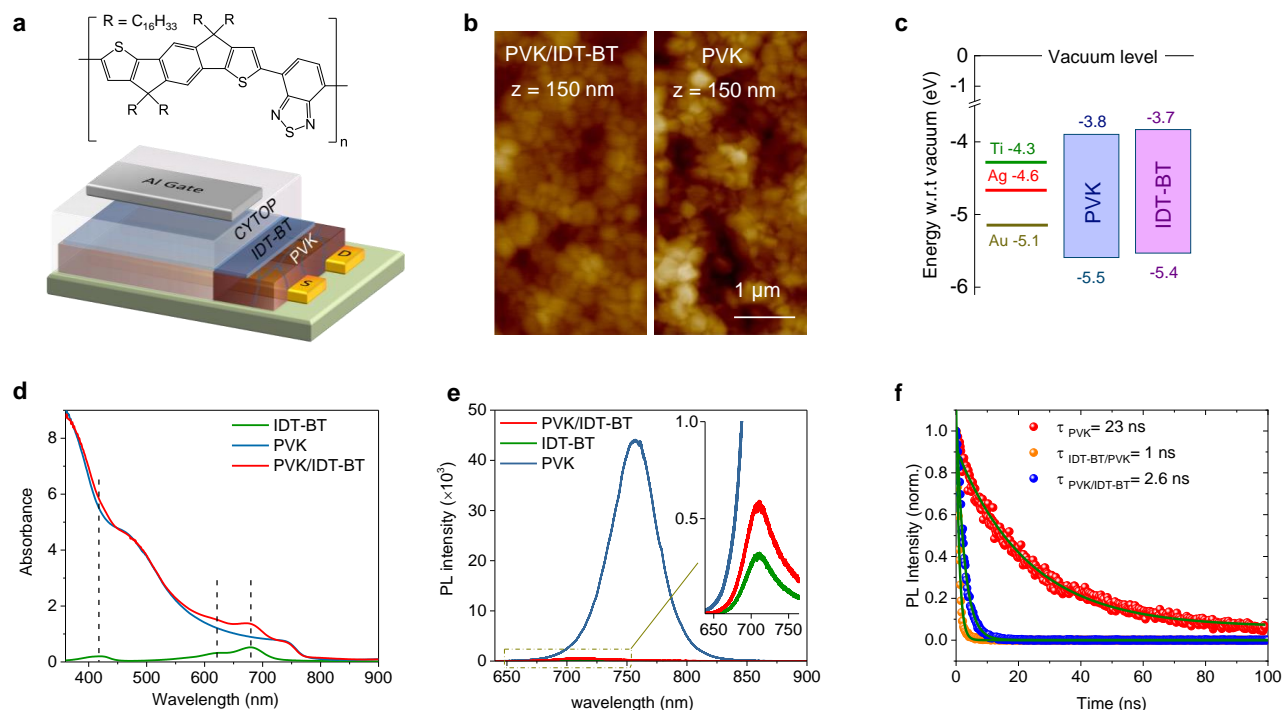


**Figure 1 Architecture and energy transfer of the IDT-BT/PVK memtransistor.** (a) Schematic of IDT-BT/PVK memtransistor with top-gate, bottom-contact configuration, in which source/drain electrodes are gold, defining the channel length ( $L$ ) = 30  $\mu m$ , width ( $W$ ) = 1000  $\mu m$ , and gate electrode is aluminium. The dielectric layer is CYTOP. The depicted molecular structure represents the IDT-BT copolymer. (b) AFM images of the IDT-BT/PVK bilayer (left) and pristine PVK (right), indicating the good coverage of IDT-BT and hinting at its penetration into the PVK film. (c) Electronic band alignment of the heterojunction with electrodes and corresponding charge transfer. (d) UV-Vis spectra for the pristine IDT-BT, PVK and IDT-BT/PVK films. (e) PL spectra of pristine IDT-BT, PVK and the bilayer. (f) TR-PL decay dynamics of neat PVK film and IDT-BT/PVK bilayer excited from either side at 532 nm, indicating charge transfer occurs on the nanosecond timescale.

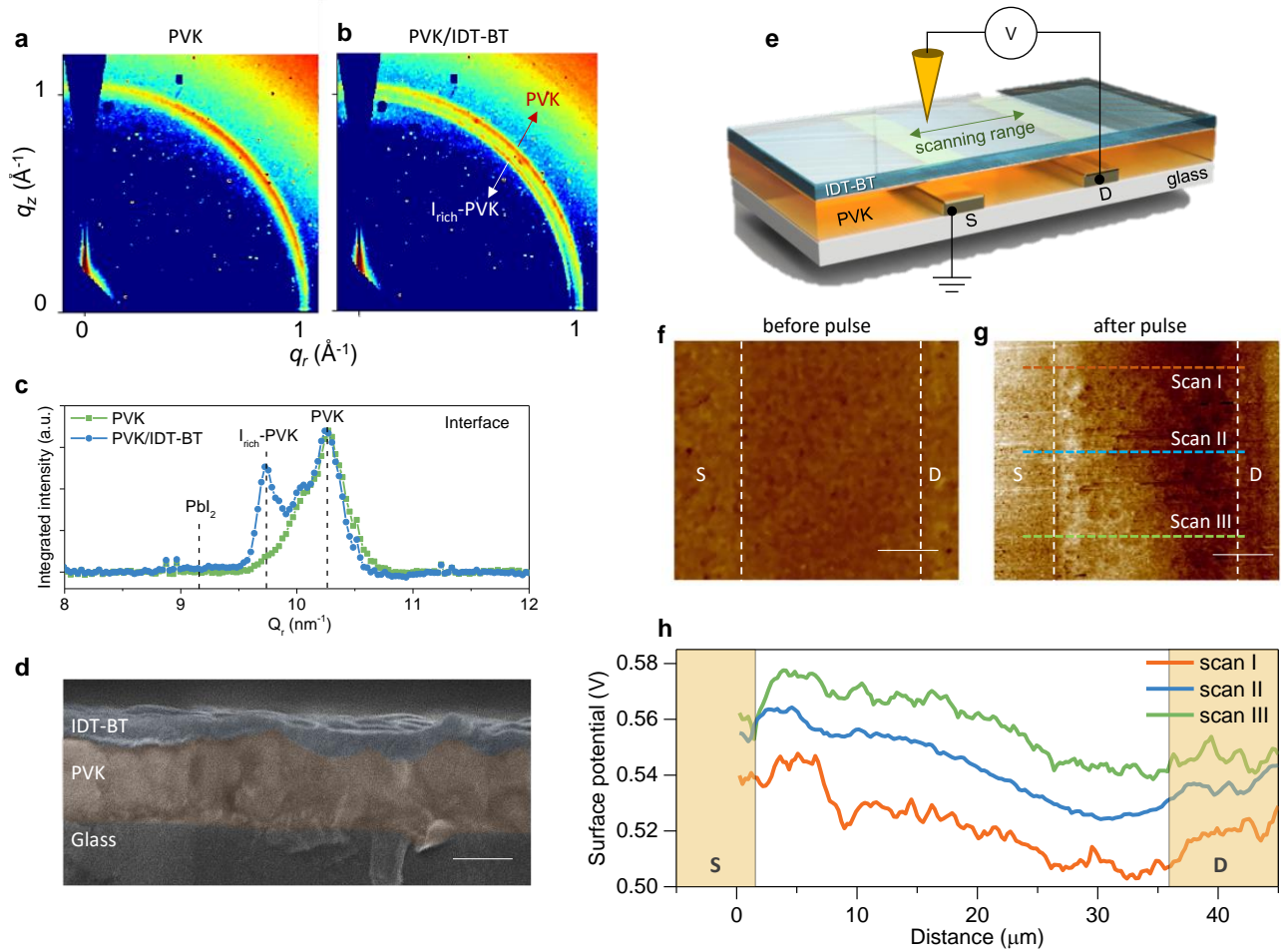


**Figure 2 Ionic conduction of the IDT-BT/PVK memtransistor.** (a) 2D-GIWAXS spectra of the pristine PVK surface with an incident angle of  $0.05^\circ$ . (b) 2D-GIWAXS spectra of the interface of IDT-BT/PVK with the same incident angle. (c) azimuthally integrated 1D plots showing the comparison of the surface of PVK w/ and w/o IDT-BT layer. (d) Cross-section SEM image of the IDT-BT/PVK stack (scale bar 100 nm). (e) Schematic of the IDT-BT/PVK heterostructure channel used for scanning Kelvin probe force microscopy (SKPFM). We note that the channel architecture is identical to that used to construct the transistors. (f, g) The SKPFM mapping before and 1 hour after the pulse (scale bar  $10 \mu\text{m}$ ). (h) Line scan of the surface potential of the heterostructure at three different positions.

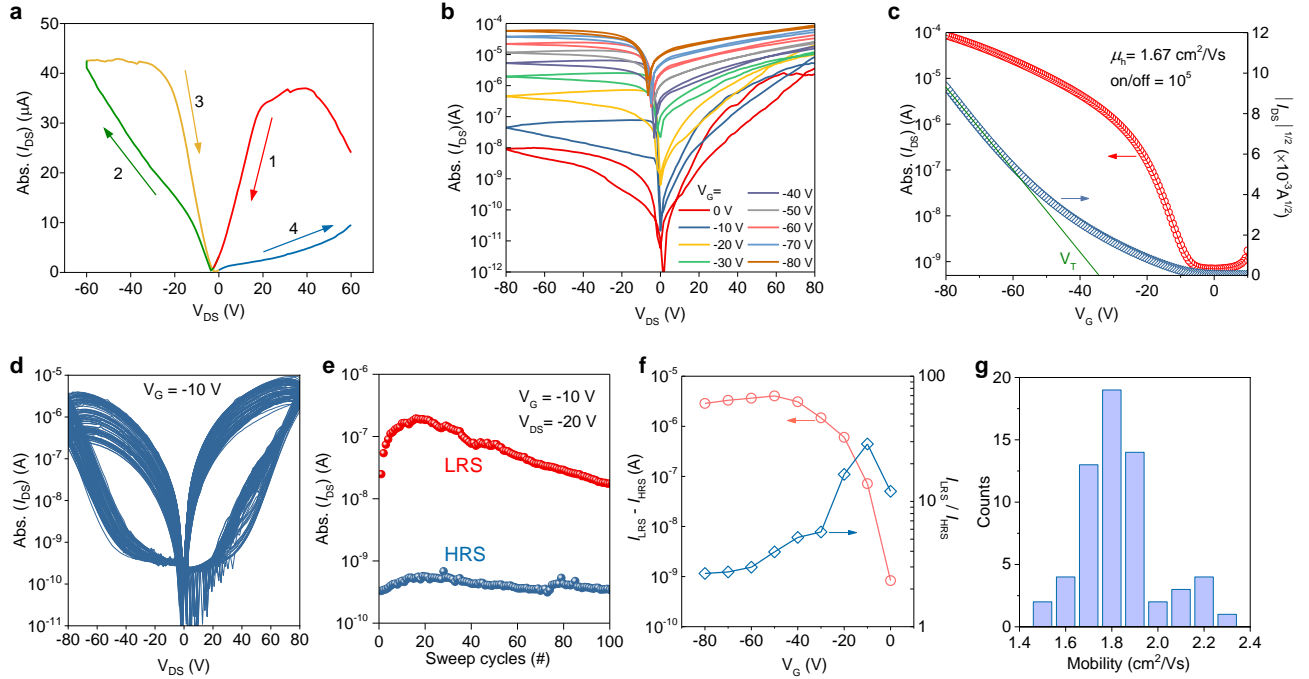


**Figure 3 Electrical characteristics of the IDT-BT/PVK memtransistor.** (a) Representative bipolar resistive switching characteristic of an IDT-BT/PVK memtransistor. The sweep direction is 1→4 at  $V_G = -60$  V. (b) Output curves of the memtransistor showing the programmable levels of switching ratio at different  $V_G$ . (c) A typical transfer curve in the low-resistance state (LRS) ( $V_{DS} = -80$  V), showing mobility of  $1.67 \text{ cm}^2/\text{Vs}$ . (d) 100 Sweep cycles of the memtransistor at  $V_G = -10$  V. (e) Endurance of the current at  $V_{DS} = -20$  V, giving a switching ratio between the low resistance state current ( $I_{LRS}$ ) and high resistance state current ( $I_{HRS}$ ) of  $\sim 10^2$ . (f) Current difference ( $I_{LRS} - I_{HRS}$ ) and switching ratio ( $I_{LRS}/I_{HRS}$ ) between LRS and HRS at different gate voltage. (g) Statistical data for the hole mobility of 64 devices, the average mobility ranges between  $1.7\text{-}1.9 \text{ cm}^2/\text{Vs}$ .

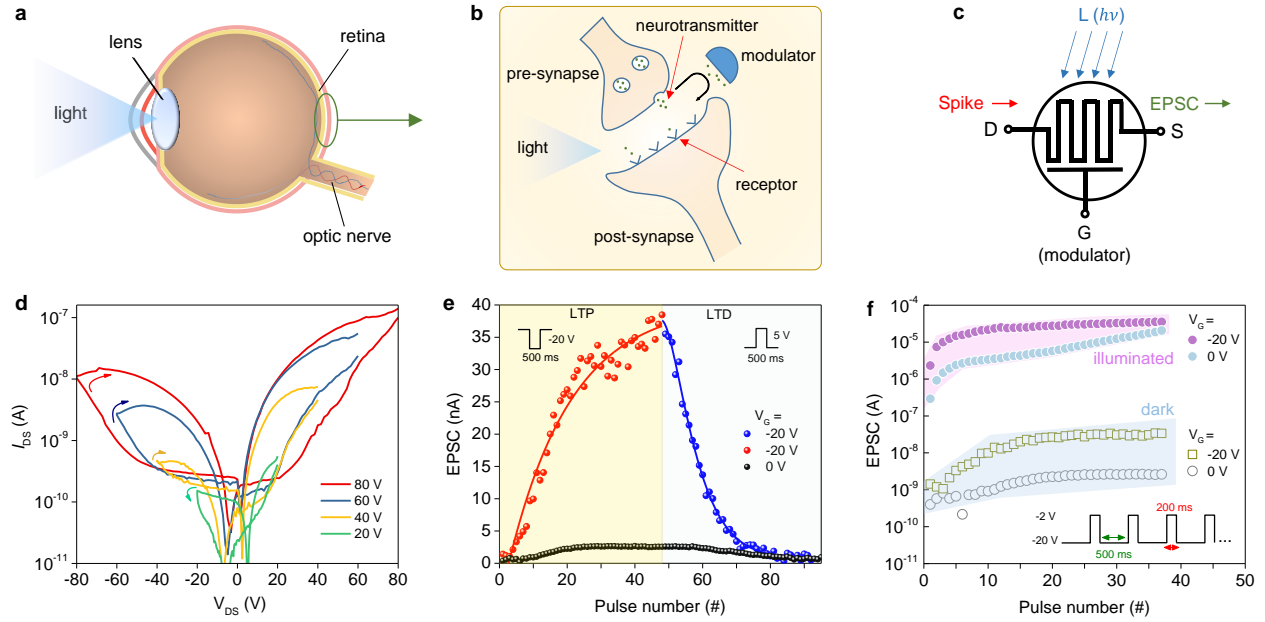


**Figure 4 Electrical and photonic plasticity of the IDT-BT/PVK memtransistor.** (a) Schematic illustration of the human visual system. (b) Schematics of the synapse in the retina. (c) electric symbol of the bio-inspired memtransistor. Drain and source terminals imitate the pre- and post-synapse, respectively. Gate terminal imitates the modulator and L symbolizes the light. (d) Pinched hysteresis loops in dark with different maximum-sweep voltages ( $V_{DS}$  from  $|\pm 20|$  V to  $|\pm 80|$  V) at  $V_G = 0$ . (e) Progression plots of the EPSC under dark as a function of the number of input pulse ( $V_{Pot} = -20$  V,  $V_{Dep} = 5$  V,  $t_{width} = 500$  ms) in dark at the different  $V_G$  of 0, and -20 V. (f) Progression plots of EPSC under light as function of time of input pulses ( $V_{Pot} = -20$  V,  $t_{width} = 500$  ms,  $t_{interval} = 200$  ms).

## ASSOCIATED CONTENT

The following files are available free of charge.

### **Supporting Information (PDF)**

Summary of the physical properties of IDT-BT (Table S1). UV-Vis absorption and PL spectrum of IDT-BT solid film (Figure S1). SEM images of PVK film and IDT-BT/PVK bilayer (Figure S2). Surface AFM images of the PVK film and IDT-BT/PVK bilayer (Figure S3). XRD and Raman spectra of single PVK layer and IDT-BT/PVK bilayer (Figure S4). Evolution of the PL emission of single PVK layer and IDT-BT/PVK bilayer (Figure S5). Molecular structure of the CYTOP polymer used as the gate dielectric (Figure S6). Electrical properties of field-effect transistors based on pristine IDT-BT (Figure S7). Operating characteristics of IDT-BT/PVK memtransistors (Figure S8). Schematic depiction of the operating principles of the IDT-BT/PVK memtransistor (Figure S9). GIWAXS spectra of PVK film and IDT-BT/PVK bilayer (Figure S10). AFM and KPFM of the bilayer (Figure S11). Temperature dependent transport characteristics of the IDT-BT/PVK memtransistors (Figure S12). Output curves of memtransistor based on Ti source/drain electrodes (Figure S13). Thickness dependent operating characteristics of IDT-BT/PVK memtransistors (Figure S14). Retention characteristics of the HRS and LRS currents (Figure S15). Schematic mechanism (Figure S16). GIWAXS data obtained for perovskite layers with different halides and the corresponding device output curves (Figure S17).

## AUTHOR INFORMATION

Dr. C. Ma, Dr. H. Chen, Dr. E. Yengel, Dr. H. Faber, Dr. J. I. Khan, K. Loganathan, Y. Lin, Dr. W. Zhang, Prof. F. Laquai, Prof. I. McCulloch, Prof. T. D. Anthopoulos

King Abdullah University of Science and Technology (KAUST)

KAUST Solar Center

Thuwal 23955-6900, Saudi Arabia

Dr. R. Li

National Synchrotron Light Source II

Brookhaven National Laboratory

Upton, New York 11973, United States

### **Corresponding Author**

Thomas D. Anthopoulos\*

King Abdullah University of Science and Technology (KAUST)

KAUST Solar Center

Thuwal 23955-6900, Saudi Arabia

E-mail: [thomas.anthopoulos@kaust.edu.sa](mailto:thomas.anthopoulos@kaust.edu.sa)

### **Author Contributions**

CM and TDA conceived the idea and written the first draft of the manuscript. CM, HF and EY carried out the electrical and optoelectronic measurements. CM carried out AFM, SKPFM, steady PL, Raman spectrum, UV-Vis spectrum, SEM, and XRD measurements. HC and WZ synthesized the IDT-BT and performed PESA measurements. RL and MCT performed the GIWAXS and analyzed the data. JIK carried out the TR-PL measurements. KL and YL contributed the device fabrication. All authors discussed the results and contributed to the writing of the paper.

## Funding Sources

This publication is based upon work supported by the King Abdullah University of Science and Technology (KAUST) Office of Sponsored Research (OSR) under Award No: OSR-2018-CARF/CCF-3079.

## REFERENCES

1. Lee, Y.; Lee, T. W., Organic Synapses for Neuromorphic Electronics: From Brain-Inspired Computing to Sensorimotor Nervetronics. *Acc. Chem. Res.* **2019**, *52* (4), 964-974.
2. Abbott, L. F.; Regehr, W. G., Synaptic Computation. *Nature* **2004**, *431* (7010), 796-803.
3. Yang, J. J. S.; Strukov, D. B.; Stewart, D. R., Memristive Devices for Computing. *Nat. Nanotechnol.* **2013**, *8* (1), 13-24.
4. Kim, K. M.; Zhang, J. M.; Graves, C.; Yang, J. J.; Choi, B. J.; Hwang, C. S.; Li, Z. Y.; Williams, R. S., Low-Power, Self-Rectifying, and Forming-Free Memristor with an Asymmetric Programing Voltage for a High-Density Crossbar Application. *Nano Lett.* **2016**, *16* (11), 6724-6732.
5. Kuzum, D.; Yu, S. M.; Wong, H. S. P., Synaptic Electronics: Materials, Devices and Applications. *Nanotechnology* **2013**, *24* (38), 382001.
6. Sangwan, V. K.; Lee, H. S.; Bergeron, H.; Balla, I.; Beck, M. E.; Chen, K. S.; Hersam, M. C., Multi-Terminal Memtransistors from Polycrystalline Monolayer Molybdenum Disulfide. *Nature* **2018**, *554* (7693), 500-504.
7. Prezioso, M.; Merrih-Bayat, F.; Hoskins, B. D.; Adam, G. C.; Likharev, K. K.; Strukov, D. B., Training and Operation of an Integrated Neuromorphic Network Based on Metal-Oxide Memristors. *Nature* **2015**, *521* (7550), 61-64.
8. Upadhyay, N. K.; Jiang, H.; Wang, Z. R.; Asapu, S.; Xia, Q. F.; Yang, J. J., Emerging Memory Devices for Neuromorphic Computing. *Advanced Materials Technologies* **2019**, *4* (4), 1800589.
9. Fuller, E. J.; Keene, S. T.; Melianas, A.; Wang, Z. R.; Agarwal, S.; Li, Y. Y.; Tuchman, Y.; James, C. D.; Marinella, M. J.; Yang, J. J.; Salleo, A.; Talin, A. A., Parallel Programming of An Ionic Floating-Gate Memory Array for Scalable Neuromorphic Computing. *Science* **2019**, *364* (6440), 570-574.
10. van de Burgt, Y.; Lubberman, E.; Fuller, E. J.; Keene, S. T.; Faria, G. C.; Agarwal, S.; Marinella, M. J.; Talin, A. A.; Salleo, A., A Non-Volatile Organic Electrochemical Device as A Low-Voltage Artificial Synapse for Neuromorphic Computing. *Nat. Mater.* **2017**, *16* (4), 414-418.
11. Choi, S.; Tan, S. H.; Li, Z. F.; Kim, Y.; Choi, C.; Chen, P. Y.; Yeon, H.; Yu, S. M.; Kim, J., SiGe Epitaxial Memory for Neuromorphic Computing with Reproducible High Performance Based on Engineered Dislocations. *Nat. Mater.* **2018**, *17* (4), 335-340.
12. Herz, L. M., Charge-Carrier Mobilities in Metal Halide Perovskites: Fundamental Mechanisms and Limits. *Acs Energy Letters* **2017**, *2* (7), 1539-1548.



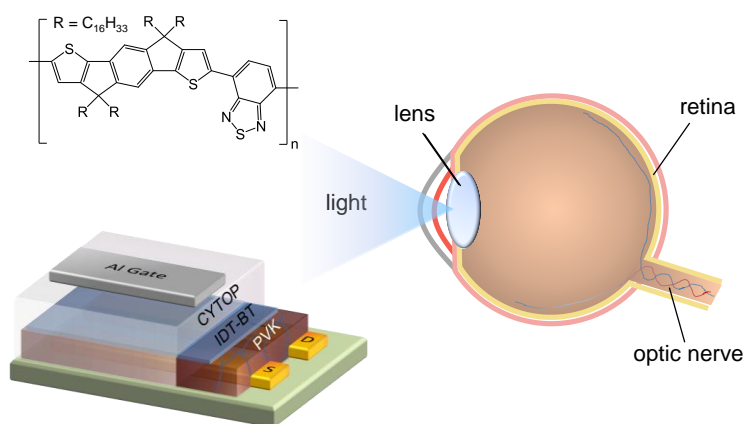
13. Jeon, N. J.; Noh, J. H.; Kim, Y. C.; Yang, W. S.; Ryu, S.; Seok, S. I., Solvent Engineering for High-Performance Inorganic-Organic Hybrid Perovskite Solar Cells. *Nat. Mater.* **2014**, *13* (9), 897-903.
14. Green, M. A.; Ho-Baillie, A.; Snaith, H. J., The Emergence of Perovskite Solar Cells. *Nat. Photonics* **2014**, *8* (7), 506-514.
15. Ahmadi, M.; Wu, T.; Hu, B., A Review on Organic-Inorganic Halide Perovskite Photodetectors: Device Engineering and Fundamental Physics. *Adv. Mater.* **2017**, *29* (41), 1605242.
16. Xu, W. D.; Hu, Q.; Bai, S.; Bao, C. X.; Miao, Y. F.; Yuan, Z. C.; Borzda, T.; Barker, A. J.; Tyukalova, E.; Hu, Z. J.; Kawecki, M.; Wang, H. Y.; Yan, Z. B.; Liu, X. J.; Shi, X. B.; Uvdal, K.; Fahlman, M.; Zhang, W. J.; Duchamp, M.; Liu, J. M.; Petrozza, A.; Wang, J. P.; Liu, L. M.; Huang, W.; Gao, F., Rational Molecular Passivation for High-Performance Perovskite Light-Emitting Diodes. *Nat. Photonics* **2019**, *13* (6), 418-424.
17. Chin, X. Y.; Cortecchia, D.; Yin, J.; Bruno, A.; Soci, C., Lead Iodide Perovskite Light-Emitting Field-Effect Transistor. *Nat. Commun.* **2015**, *6*, 7383.
18. Choi, J.; Park, S.; Lee, J.; Hong, K.; Kim, D. H.; Moon, C. W.; Park, G. D.; Suh, J.; Hwang, J.; Kim, S. Y.; Jung, H. S.; Park, N. G.; Han, S.; Nam, K. T.; Jang, H. W., Organolead Halide Perovskites for Low Operating Voltage Multilevel Resistive Switching. *Adv. Mater.* **2016**, *28* (31), 6562-6567.
19. Xiao, Z. G.; Yuan, Y. B.; Shao, Y. C.; Wang, Q.; Dong, Q. F.; Bi, C.; Sharma, P.; Gruverman, A.; Huang, J. S., Giant Switchable Photovoltaic Effect in Organometal Trihalide Perovskite Devices. *Nat. Mater.* **2015**, *14* (2), 193-198.
20. Senanayak, S. P.; Yang, B. Y.; Thomas, T. H.; Giesbrecht, N.; Huang, W. C.; Gann, E.; Nair, B.; Goedel, K.; Guha, S.; Moya, X.; McNeill, C. R.; Docampo, P.; Sadhanala, A.; Friend, R. H.; Sirringhaus, H., Understanding Charge Transport in Lead Iodide Perovskite Thin-Film Field-Effect Transistors. *Science Advances* **2017**, *3* (1), e1601935.
21. Calado, P.; Telford, A. M.; Bryant, D.; Li, X. E.; Nelson, J.; O'Regan, B. C.; Barnes, P. R. F., Evidence for Ion Migration in Hybrid Perovskite Solar Cells with Minimal Hysteresis. *Nat. Commun.* **2016**, *7*, 13831.
22. Kim, G. Y.; Senocrate, A.; Yang, T. Y.; Gregori, G.; Gratzel, M.; Maier, J., Large Tunable Photoeffect on Ion Conduction in Halide Perovskites and Implications for Photodecomposition. *Nat. Mater.* **2018**, *17* (5), 445-449.
23. Feldmann, J.; Youngblood, N.; Wright, C. D.; Bhaskaran, H.; Pernice, W. H. P., All-Optical Spiking Neurosynaptic Networks with Self-Learning Capabilities. *Nature* **2019**, *569* (7755), 208-214.
24. Johnston, M. B.; Herz, L. M., Hybrid Perovskites for Photovoltaics: Charge-Carrier Recombination, Diffusion, and Radiative Efficiencies. *Acc. Chem. Res.* **2016**, *49* (1), 146-154.
25. D'Innocenzo, V.; Grancini, G.; Alcocer, M. J. P.; Kandada, A. R. S.; Stranks, S. D.; Lee, M. M.; Lanzani, G.; Snaith, H. J.; Petrozza, A., Excitons versus Free Charges in Organolead Tri-Halide Perovskites. *Nat. Commun.* **2014**, *5*, 3586.
26. Venkateshvaran, D.; Nikolka, M.; Sadhanala, A.; Lemaire, V.; Zelazny, M.; Kepa, M.; Hurhangee, M.; Kronemeijer, A. J.; Pecunia, V.; Nasrallah, I.; Romanov, I.; Broch, K.; McCulloch, I.; Emin, D.; Olivier, Y.; Cornil, J.; Beljonne, D.; Sirringhaus, H., Approaching Disorder-Free Transport in High-Mobility Conjugated Polymers. *Nature* **2014**, *515* (7527), 384-388.

27. Zhang, W. M.; Smith, J.; Watkins, S. E.; Gysel, R.; McGehee, M.; Salleo, A.; Kirkpatrick, J.; Ashraf, S.; Anthopoulos, T.; Heeney, M.; McCulloch, I., Indacenodithiophene Semiconducting Polymers for High-Performance, Air-Stable Transistors. *J Am Chem Soc* **2010**, *132* (33), 11437-11439.
28. Ma, C.; Shi, Y. M.; Hu, W. J.; Chiu, M. H.; Liu, Z. X.; Bera, A.; Li, F.; Wang, H.; Li, L. J.; Wu, T., Heterostructured WS<sub>2</sub>/CH<sub>3</sub>NH<sub>3</sub>PbI<sub>3</sub> Photoconductors with Suppressed Dark Current and Enhanced Photodetectivity. *Adv. Mater.* **2016**, *28* (19), 3683-3689.
29. Lin, Y. H.; Pattanasattayavong, P.; Anthopoulos, T. D., Metal-Halide Perovskite Transistors for Printed Electronics: Challenges and Opportunities. *Adv. Mater.* **2017**, *29* (46), 1702838.
30. Eames, C.; Frost, J. M.; Barnes, P. R. F.; O'Regan, B. C.; Walsh, A.; Islam, M. S., Ionic Transport in Hybrid Lead Iodide Perovskite Solar Cells. *Nat. Commun.* **2015**, *6*, 7497.
31. Zheng, G. H. J.; Zhu, C.; Ma, J. Y.; Zhang, X. N.; Tang, G.; Li, R. G.; Chen, Y. H.; Li, L.; Hu, J. S.; Hong, J. W.; Chen, Q.; Gao, X. Y.; Zhou, H. P., Manipulation of Facet Orientation in Hybrid Perovskite Polycrystalline Films by Cation Cascade. *Nat. Commun.* **2018**, *9*, 2793.
32. Wang, K.; Tang, M. C.; Dang, H. X.; Munir, R.; Barrit, D.; De Bastiani, M.; Aydin, E.; Smilgies, D. M.; De Wolf, S.; Amassian, A., Kinetic Stabilization of the Sol-Gel State in Perovskites Enables Facile Processing of High-Efficiency Solar Cells. *Adv. Mater.* **2019**, *31* (32), 1808357.
33. Shao, Y. C.; Fang, Y. J.; Li, T.; Wang, Q.; Dong, Q. F.; Deng, Y. H.; Yuan, Y. B.; Wei, H. T.; Wang, M. Y.; Gruverman, A.; Shielda, J.; Huang, J. S., Grain Boundary Dominated Ion Migration in Polycrystalline Organic-Inorganic Halide Perovskite Films. *Energ Environ Sci* **2016**, *9* (5), 1752-1759.
34. Wei, L. Y.; Ma, W.; Lian, C.; Meng, S., Benign Interfacial Iodine Vacancies in Perovskite Solar Cells. *J. Phys. Chem. C* **2017**, *121* (11), 5905-5913.
35. Zhu, X. J.; Lee, J.; Lu, W. D., Iodine Vacancy Redistribution in Organic-Inorganic Halide Perovskite Films and Resistive Switching Effects. *Adv. Mater.* **2017**, *29* (29), 1700527.
36. Li, C.; Guerrero, A.; Huettner, S.; Bisquert, J., Unravelling The Role of Vacancies in Lead Halide Perovskite Through Electrical Switching of Photoluminescence. *Nat. Commun.* **2018**, *9*, 5113.
37. Zhou, F. C.; Zhou, Z.; Chen, J. W.; Choy, T. H.; Wang, J. L.; Zhang, N.; Lin, Z. Y.; Yu, S. M.; Kang, J. F.; Wong, H. S. P.; Chai, Y., Optoelectronic Resistive Random Access Memory for Neuromorphic Vision Sensors. *Nat. Nanotechnol.* **2019**, *14* (8), 776-782.
38. Tanaka, M.; Tachibana, M., Independent Control of Reciprocal and Lateral Inhibition at The Axon Terminal of Retinal Bipolar Cells. *Journal of Physiology-London* **2013**, *591* (16), 3833-3851.
39. Wang, Y.; Lv, Z. Y.; Chen, J. R.; Wang, Z. P.; Zhou, Y.; Zhou, L.; Chen, X. L.; Han, S. T., Photonic Synapses Based on Inorganic Perovskite Quantum Dots for Neuromorphic Computing. *Adv. Mater.* **2018**, *30* (38), 1802883.
40. Huh, W.; Jang, S.; Lee, J. Y.; Lee, D.; Lee, D.; Lee, J. M.; Park, H. G.; Kim, J. C.; Jeong, H. Y.; Wang, G.; Lee, C. H., Synaptic Barristor Based on Phase-Engineered 2D Heterostructures. *Adv. Mater.* **2018**, *30* (35), 1801447.
41. John, R. A.; Yantara, N.; Ng, Y. F.; Narasimman, G.; Mosconi, E.; Meggiolaro, D.; Kulkarni, M. R.; Gopalakrishnan, P. K.; Nguyen, C. A.; De Angelis, F.; Mhaisalkar, S. G.;

Basu, A.; Mathews, N., Ionotronic Halide Perovskite Drift-Diffusive Synapses for Low-Power Neuromorphic Computation. *Adv. Mater.* **2018**, 30 (51), 1805454.

42. Li, D.; Liang, X. G., Neurons Mimicked by Electronics. *Nature* **2018**, 554 (7693), 472-473.

## Table of Contents



## Supporting Information

### A printed memtransistor utilizing a hybrid perovskite/organic heterojunction channel

*Chun Ma<sup>†</sup>, Hu Chen<sup>†</sup>, Emre Yengel<sup>†</sup>, Hendrik Faber<sup>†</sup>, Jafar I. Khan<sup>†</sup>, Ming-Chun Tang<sup>†</sup>, Ruipeng Li<sup>‡</sup>, Kalaivanan Loganathan<sup>†</sup>, Yuanbao Lin<sup>†</sup>, Weimin Zhang<sup>†</sup>, Frédéric Laquai<sup>†</sup>, Iain McCulloch<sup>†</sup> & Thomas D. Anthopoulos<sup>†\*</sup>*

<sup>†</sup> King Abdullah University of Science and Technology (KAUST), KAUST Solar Center, Thuwal 23955-6900, Saudi Arabia.

E-mail: [thomas.anthopoulos@kaust.edu.sa](mailto:thomas.anthopoulos@kaust.edu.sa)

<sup>‡</sup> National Synchrotron Light Source II, Brookhaven National Laboratory  
Upton, New York 11973, United States

**Table S1.** Summary of the physical properties of the IDT-BT polymer.

Polymer	M <sub>n</sub> (kDa)/M <sub>w</sub> (kDa) <sup>a</sup>	λ <sub>max</sub> /nm (thin film) <sup>b</sup>	E <sub>opt.gap</sub> <sup>c</sup>	IP (eV) <sup>d</sup>	EA (eV) <sup>e</sup>
IDT-BT	58.3/95.3	666	1.7	-5.4	-3.7

<sup>a</sup> Molar mass averages of the number (M<sub>n</sub>) and molar mass averages of the weight (M<sub>w</sub>).

<sup>b</sup> Maximum absorption wavelength (λ<sub>max</sub>) of solid film.

<sup>c</sup> Optical band gap (E<sub>opt.gap</sub>) obtained from the onset value of absorption in pristine film.

<sup>d</sup> Ionization potential (IP) measured via Photo-Electron Spectroscopy in Air (PESA).

<sup>e</sup> Electron affinity (EA) calculated from E<sub>opt.gap</sub> and IP.

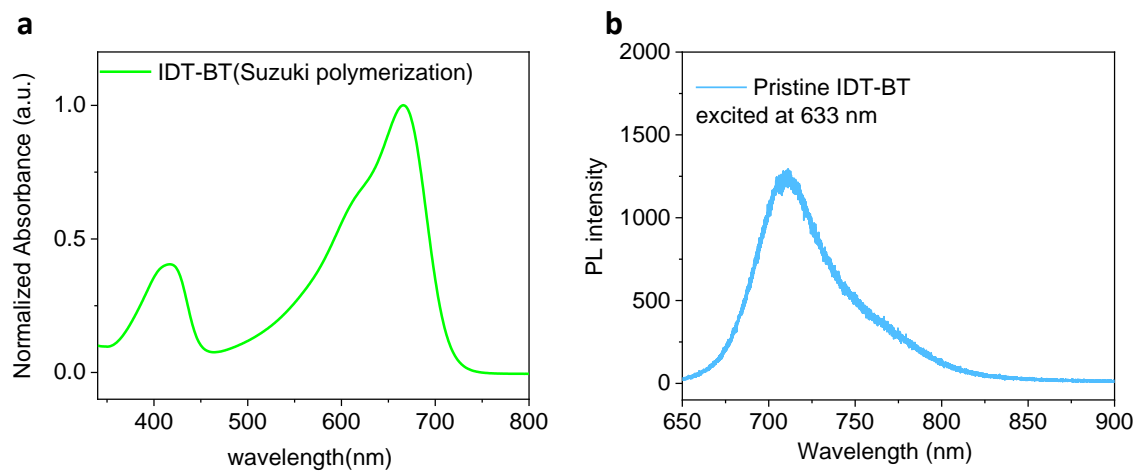


**Figure S1.** UV-vis absorption and photoluminescence (PL) spectra measured for pristine IDT-BT film.

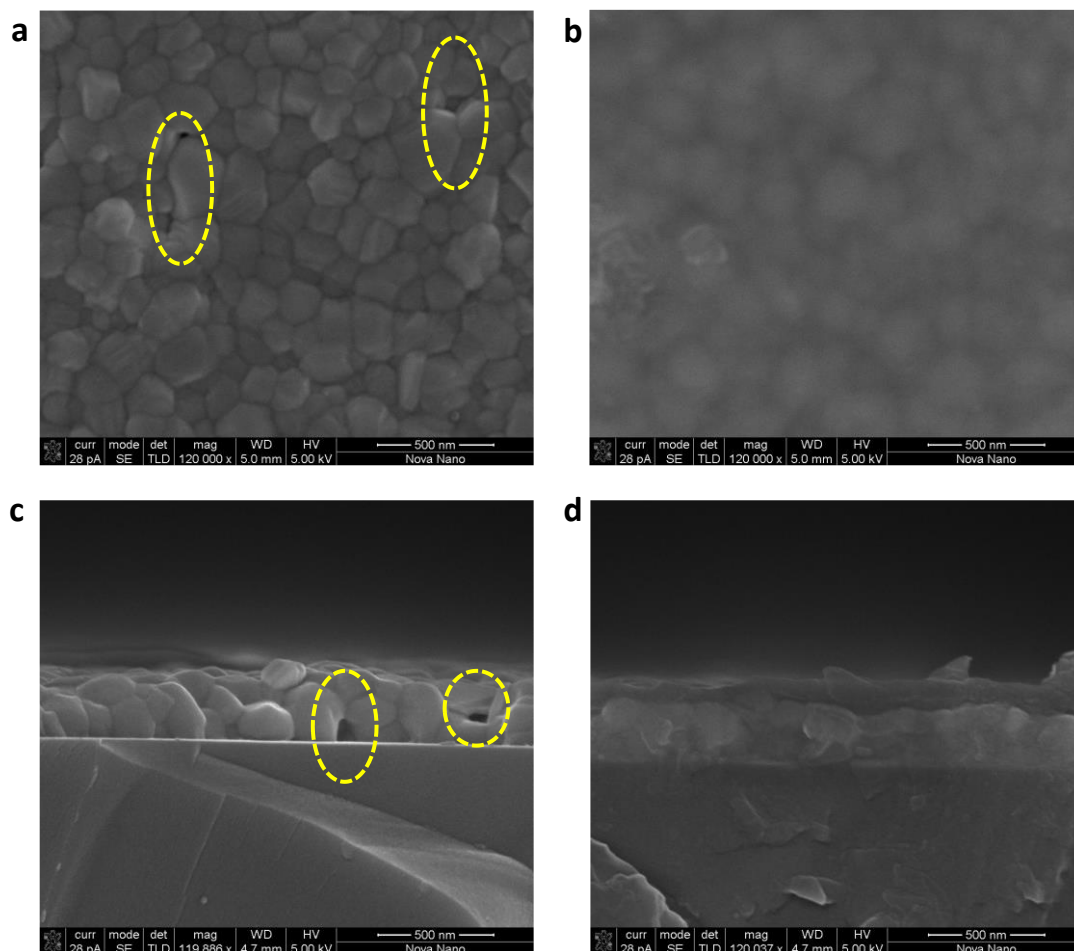


**Figure S2.** (a, b) Top-view SEM images of the pristine PVK film and IDT-BT/PVK bilayer. (c, d) Cross-section of the SEM images from the pristine PVK film and IDT-BT/PVK bilayer, respectively. The circles in (c) highlight the presence of pinholes present in the pristine PVK layer. The latter features are absent from the PVK/IDT-BT bilayer (d) due to the filling effect induced by the polymer when coated atop the PVK.

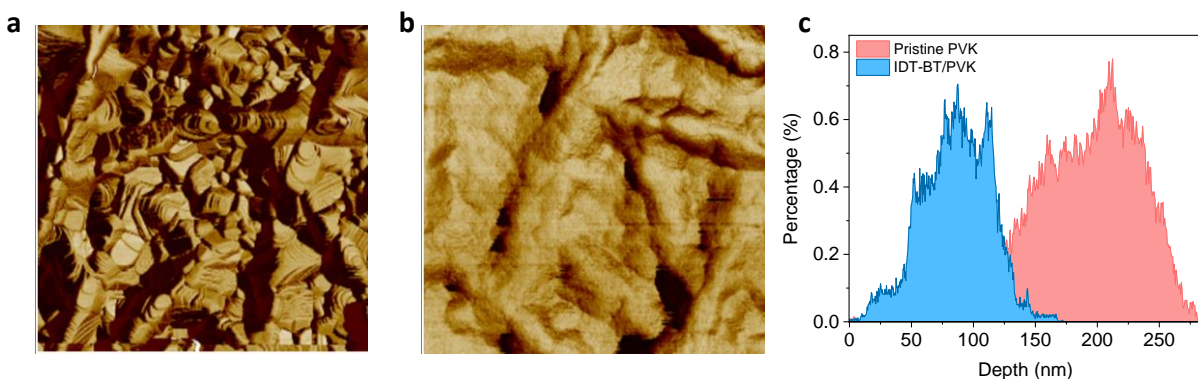


**Figure S3.** (a, b) AFM phase images ( $2\mu\text{m} \times 2\mu\text{m}$ ) of the pristine PVK film and IDT-BT/PVK bilayer, respectively. Pristine PVK films appear to be polycrystalline with high surface roughness. (c) Depth (height) histograms obtained from the topography AFM images for the pristine PVK and IDT-BT/PVK bilayers. The surface of the IDT-BT/PVK bilayer is significantly smoother with the whole distribution shifted towards lower depth (height) values.

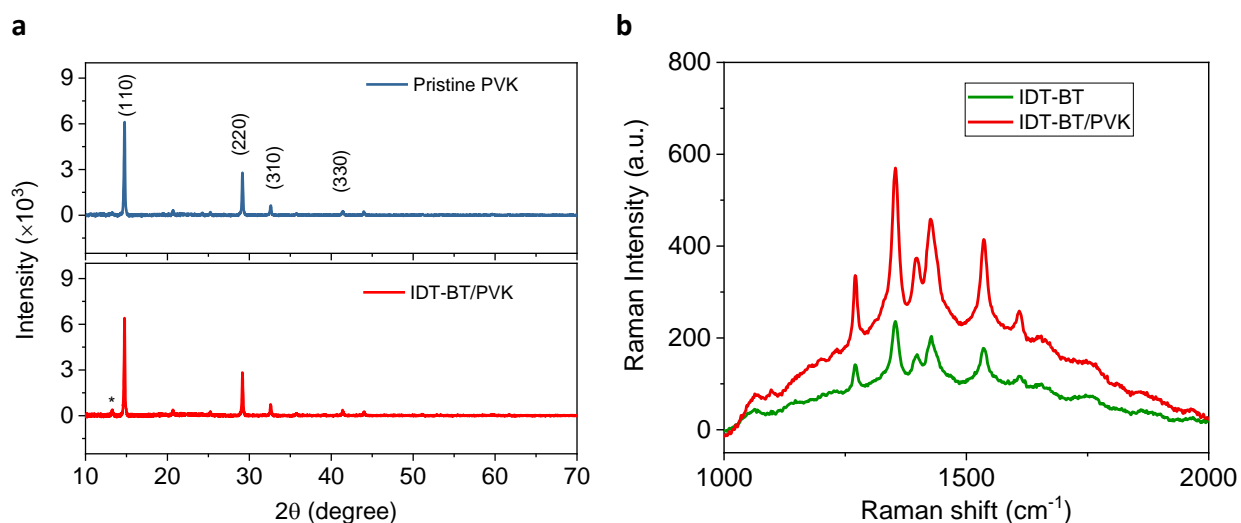


**Figure S4.** (a) XRD patterns obtained for the pristine PVK film and IDT-BT/PVK bilayer. (b) Raman spectra of the pristine PVK film and IDT-BT/PVK bilayer. The fingerprint peaks of IDT-BT show no shift when deposited atop the PVK layer indicating no chemical interaction.

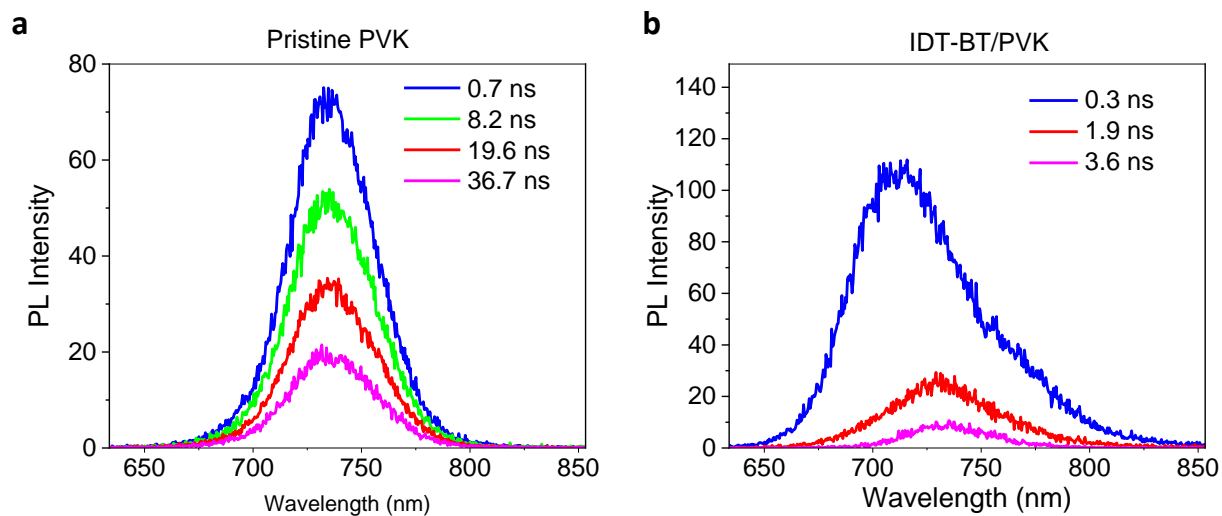


**Figure S5.** (a) Time-dependent evolution of steady PL spectra measured for the pristine PVK, and (b) the IDT-BT/PVK bilayer. The results confirm that energy transfer occurs in nanosecond scale.

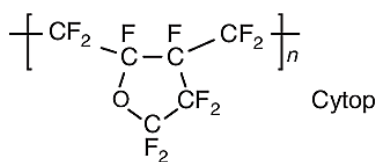


**Figure S6.** Molecular structure of CYTOP.



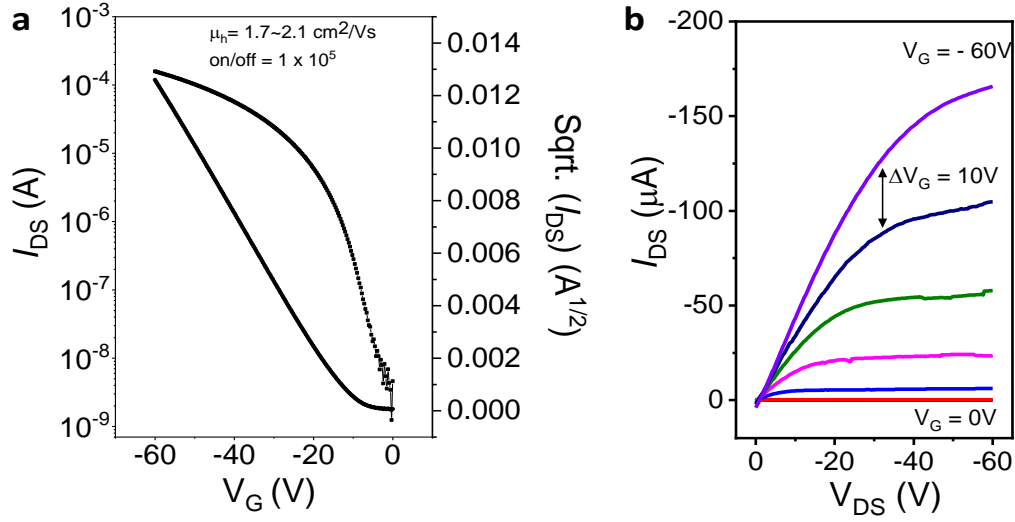


**Figure S7.** Representative transfer (a) and output (b) characteristics obtained from a pristine IDT-BT transistor. The maximum hole mobility and current on/off ratio obtained from the transistor were  $2.1 \text{ cm}^2/\text{Vs}$  and  $10^5$ , respectively.

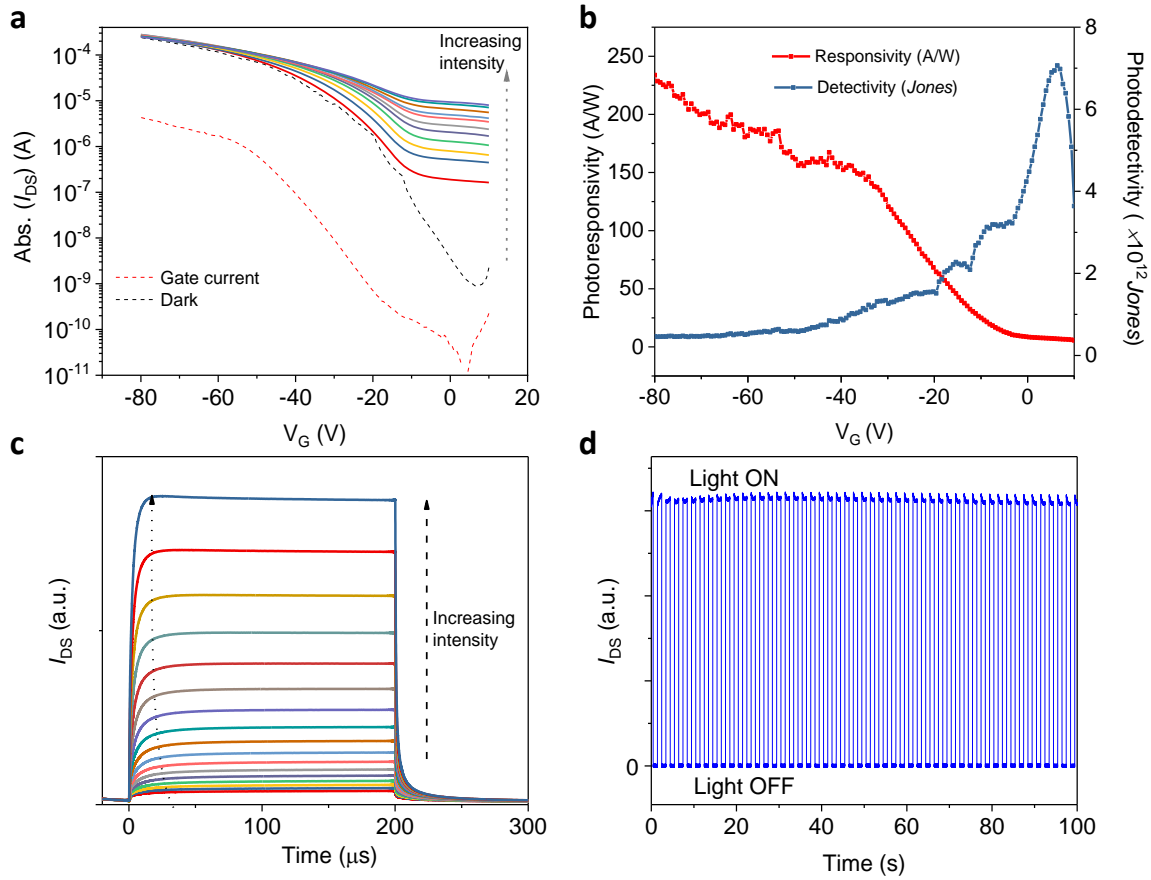


**Figure S8. Photoresponse of the IDT-BT/PVK memtransistor.** (a) Transfer characteristics of an IDT-BT/PVK memtransistor illuminated with different light intensities (from dark to 7.2 mW/cm<sup>2</sup>). The black dash line represents the transfer curve in the dark, and the red dash line represents the leakage ( $I_G$ ) current during the  $V_G$  sweeping with  $V_{DS} = -80$  V. (b) calculated photoresponsivity and photodetectivity at different  $V_G$ . The incident light intensity was fixed at 1 mW/cm<sup>2</sup>. The highest photoresponsivity (227 A/W) was achieved at  $V_G = -80$  V, while the highest photodetectivity was achieved at  $V_G = 6$  V. (c) Transient photocurrent at a light pulse frequency of 2.5 kHz with different white light intensity (from 2 to 53.9 mW/cm<sup>2</sup>). (d) photo-switching characteristics of the device under alternating dark and light illumination (630 nm, 0.21 mW/cm<sup>2</sup>).

By comparing the transfer characteristics measured in the dark with those under illumination (1 mW/cm<sup>2</sup>), the photoresponsivity ( $R$ ) and photodetectivity ( $D$ ) were calculated (Figure S8b) using:

$$R = \frac{I_{ph}}{P_{opt}} = \frac{I_{illum} - I_{dark}}{E_{opt} \cdot a} \quad (S1)$$

where,  $I_{illum}$  is the current under illumination,  $I_{dark}$  is the current in dark,  $E_{opt}$  is the illumination intensities measured by the power sensors and  $a$  is the device area. The device area for a transistor is the area defined by the channel length and width, while for diodes it is defined by the overlap between two electrodes:

$$D^* = \frac{\sqrt{a \cdot f_B}}{NEP} = \frac{\sqrt{a \cdot f_B} \cdot R}{S_{noise}} \quad (S2)$$

Here,  $a$  is the device area,  $f_B$  is the bandwidth of the device,  $NEP$  is the noise equivalent power,  $R$  is the responsivity and  $S_{noise}$  is the noise spectral density. By assuming that the shot-noise dominates:

$$i_{total} \approx i_{n,s} = \sqrt{2qI_d \Delta f} \quad (S3)$$

The detectivity ( $D^*$ ) equation can be written as:

$$D^* = \frac{R}{(2qI_d/A)^{1/2}} \quad (\text{S4})$$

A very high photoresponsivity value of 227 A/W was achieved at  $V_G = -80$  V, indicating efficient photoelectric conversion. The semiconducting IDT-BT channel was completely turned OFF in the dark at  $V_G = 6$  V while maintaining its ON state under illumination. This is the main reason why the highest photodetectivity of  $7.2 \times 10^{12}$  Jones is achieved at this biasing conditions.

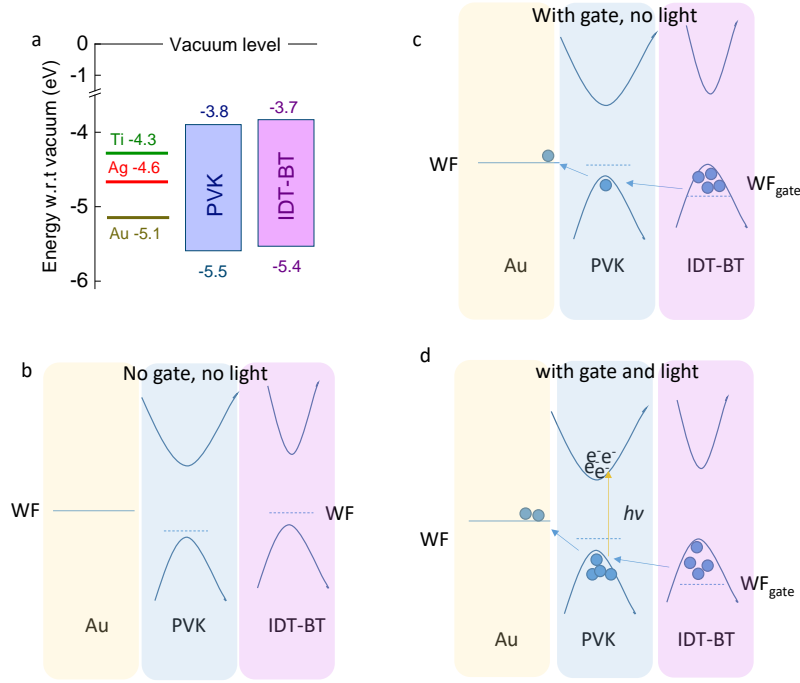


**Figure S9.** a) Energy band diagrams of the metals, PVK and IDT-BT. b) Schematic of the energy diagram of Au, PVK and IDT-BT without gate field in the dark. c) Energy band diagram of Au, PVK and IDT-BT with gate field applied in the dark. d) Energy diagram of Au, PVK and IDT-BT with gate field applied and under illumination.

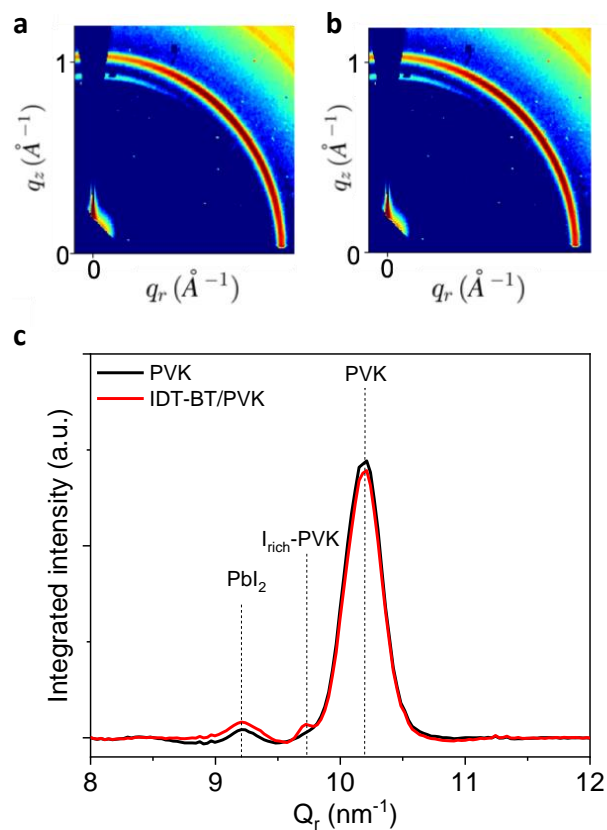


**Figure S10.** 2D-GIWAXS spectra of the pristine PVK bulk before (a) and after (b) IDT-BT deposition. Measurements were obtained using an incident angle of  $0.15^\circ$ . (c) Integrated 1D plots from GIWAXS of the bulk of PVK film and IDT-BT/PVK stack. Iodine-rich phase of perovskite can only be observed in the IDT-BT/PVK stack.

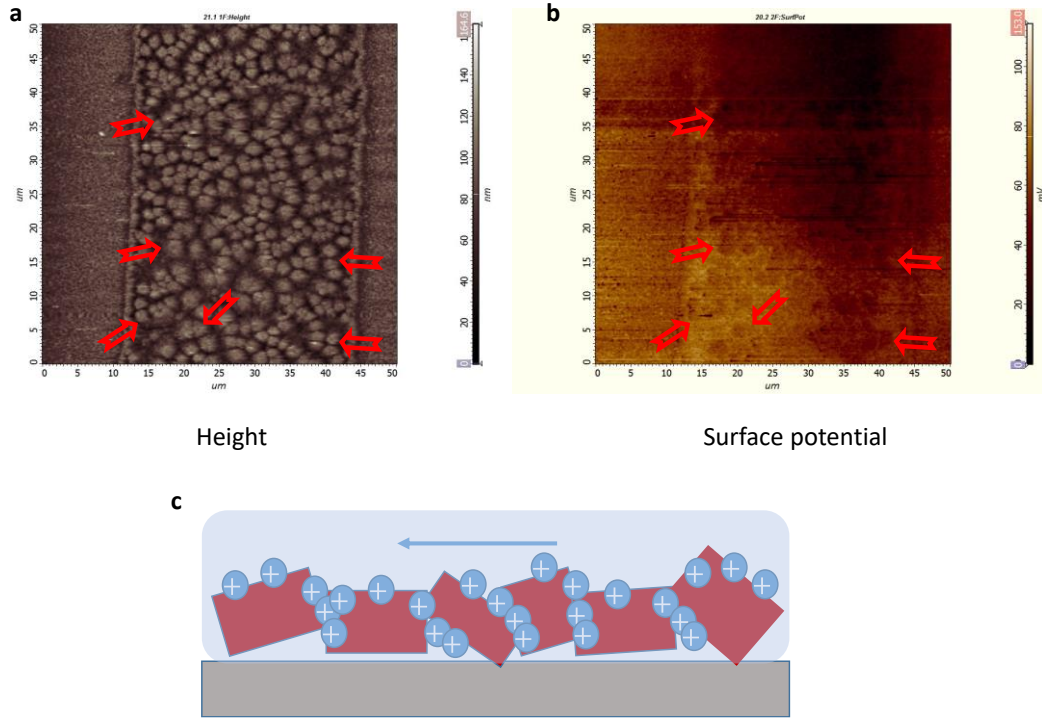


**Figure S11.** (a) Topography AFM image of the bilayer channel with source-drain electrodes visible on the sides. (b) Surface potential map of the same channel region seen in (a). Brighter regions observed around crystalline grains indicate higher surface potential. (c) Schematic of the ion distribution and migration in the layer/grains. The higher surface potential in the grain boundaries, seen in (b), suggests ions segregate in the grain boundaries and/or at the interface.

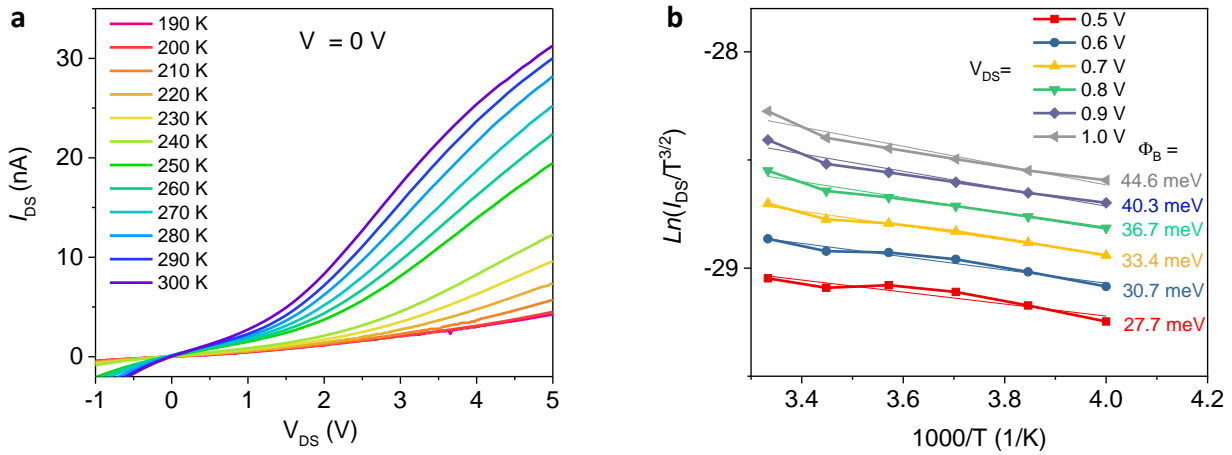


**Figure S12.** (a) Temperature-dependent charge transport measurements ( $I_{DS}$  vs.  $V_{DS}$ ) obtained in the region 190-300 K. (b) Experimental data (symbols) and theoretical fittings (lines) using the thermionic emission model, where the Schottky-barrier FETs (SB-FETs) is considered in a 2D configuration.

In the sub-threshold regime, the charge transport in Schottky-barrier FETs (SB-FETs) is dominated by thermionic emission described as:<sup>1</sup>

$$I_{DS} = A^* T^{3/2} \exp\left(\frac{\phi_b}{k_B T}\right) \left[ \exp\left(\frac{e V_{DS}}{k_B T}\right) - 1 \right] \quad (S5)$$

where,  $A^*$  is the 2D equivalent Richardson constant. The term  $T^{3/2}$  comes from the 2D model (as opposed to  $T^2$  in three dimensions). At low bias, we can extract  $\phi_b$  from the relationship of  $\ln(I/T^{3/2})$  with  $1/T$ .

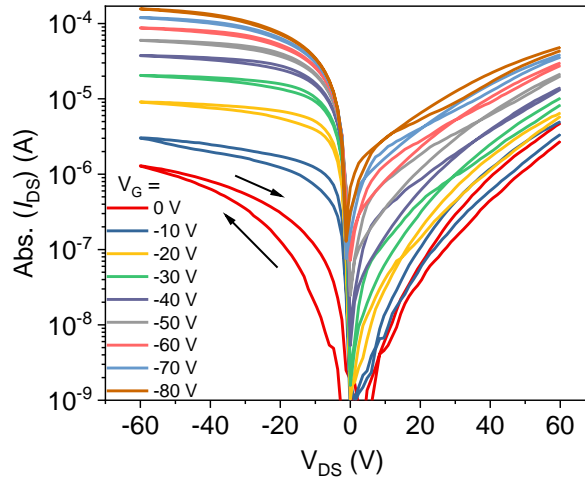


**Figure S13.** Representative set of output characteristics measured at different gate biases for an IDT-BT/PVK memtransistor with Ti electrodes.

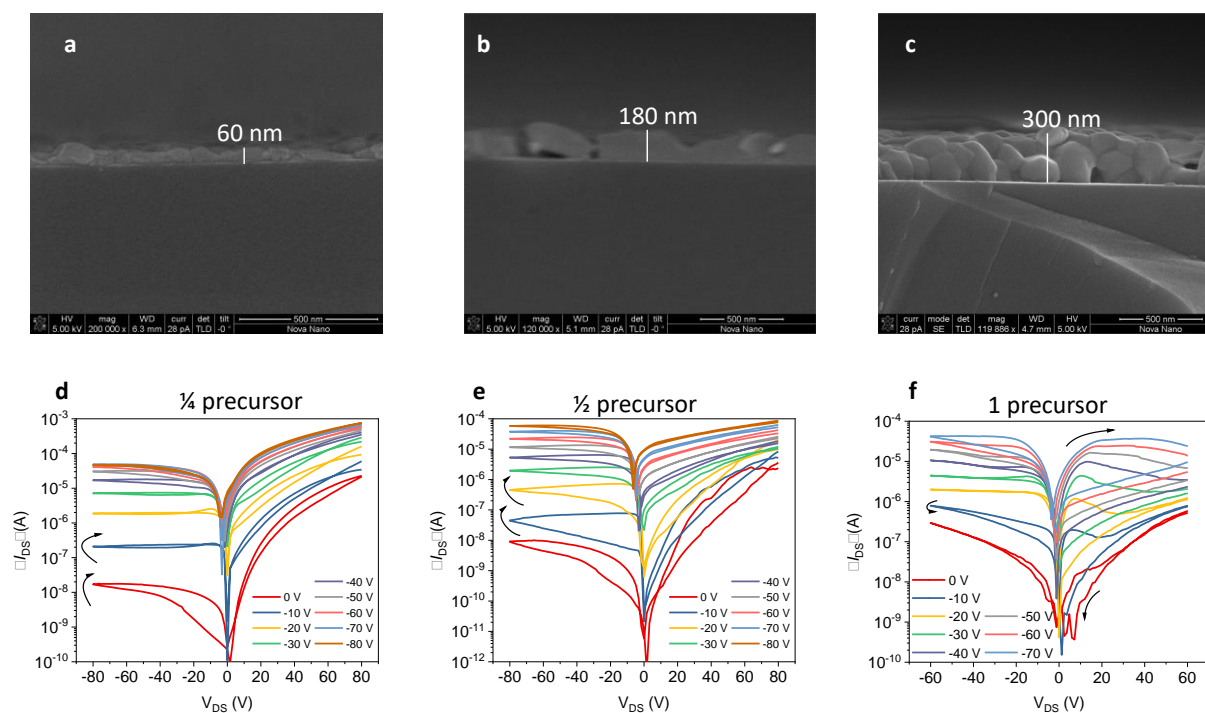


**Figure S14.** A series of cross-sectional SEM images of pristine PVK layers processed from formulations with different precursor concentrations; 0.2M (a), 0.4M (b), and 0.8M (c). (d-f) Corresponding output characteristics demonstrating the importance of the thickness of PVK layer for proper memtransistor operation.

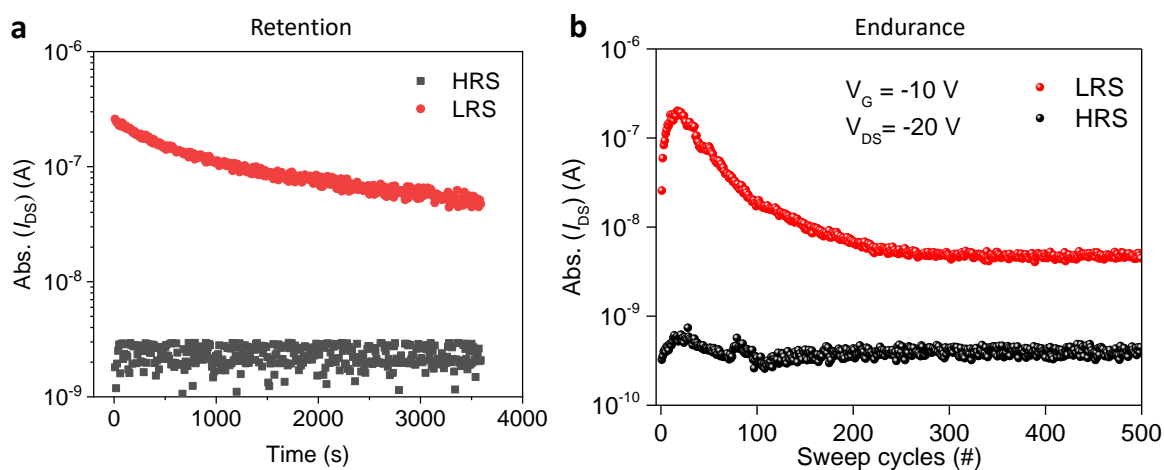


**Figure S15.** a) Retention of the HRS and LRS currents at  $V_{DS} = -10$  V,  $V_G = -10$  V over a 2-h period in the dark. b) Endurance of the HRS and LRS.

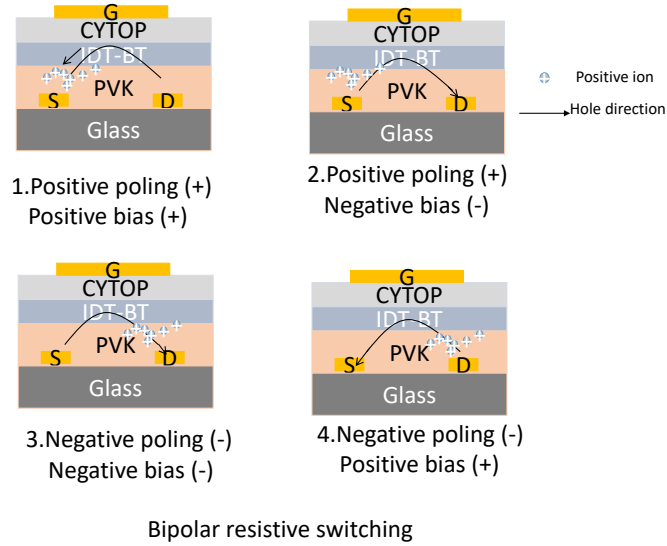


**Figure S16.** Series of schematics illustrating the ion migration and carrier transport across an IDT-BT/PVK memtransistor, resulting in a bipolar resistive switching behaviour observed.

In region 1, positive poling ( $V_p > 20$  V) was applied to drain electrode before measuring the current ( $I_{DS}$ ) at positive  $V_{DS}$  of  $>0$ . As previous studies showed, the iodine vacancy ( $V_I$ ) is the dominant ion in PVK films due to its lower formation energy and higher ionic mobility. Under these bias conditions positive ions ( $V_I$ ) are repelled away from the drain terminal, forming a lower concentration of iodine vacancy ( $V_I$ ) around the drain terminal leading to n-type self-doping of the region.<sup>2</sup> The majority carriers (holes) can then be easier injected from the Au electrodes to the valence band of the PVK layer due the reduced Schottky barrier height. In region 2, positive poling remains although the  $I_{DS}$  is measured at  $V_{DS} < 0$ . The PVK film remains p-doped at the drain terminal, which reduces the  $I_{DS}$  and rectifies the current in a similar manner to a PN junction. In region 3, the negative poling induces ion migration, and  $V_I$  accumulates in the vicinity of the drain terminal. Application of a reverse bias flips the PN junction configuration to NP. Similarly,  $I_{DS}$  reduces in region 4.



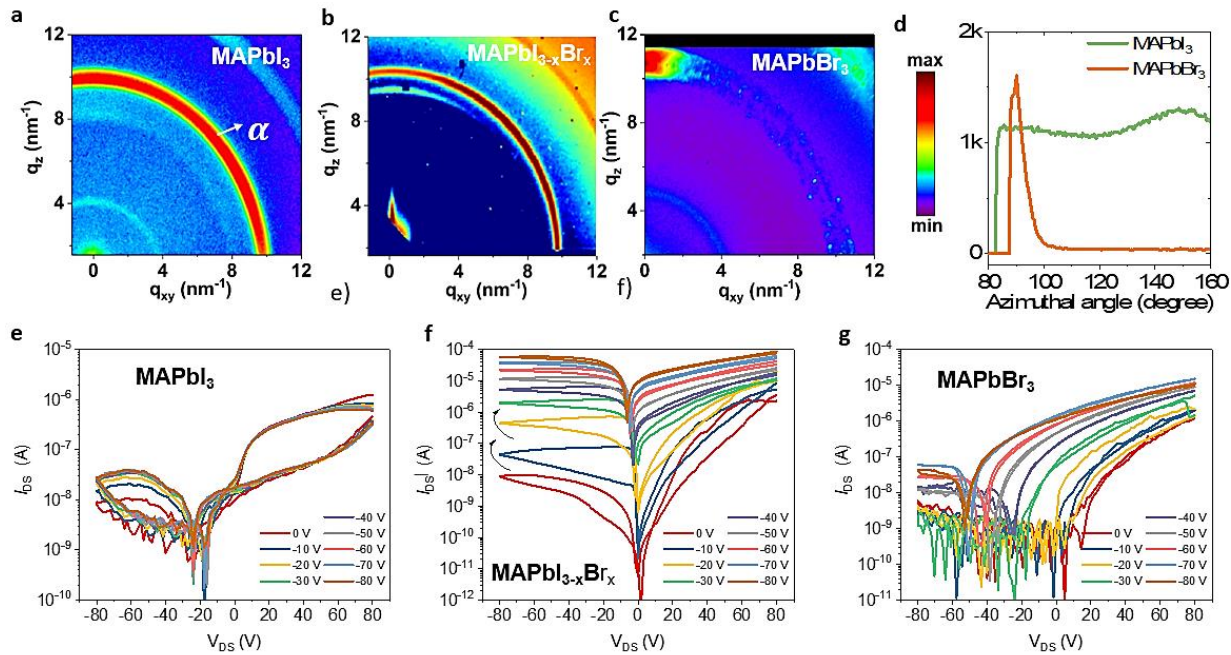


**Figure S17.** (a,b,c) 2D-GIWAXS spectra of the pristine PVK with different bromide concentrations. The spectra were measured at an incident angle of  $0.15^\circ$ , revealing the crystalline nature (bulk region) of the PVK layer. (d) The integrated intensities at different azimuthal angle, showing that the MAPbBr<sub>3</sub> is more crystalline with an out-of-plane growth direction. (e,f,g) Corresponding double sweep output curves, indicating iodine vacancies play a key role on the overall device operation. In b and f the stoichiometry of the halide concentration was fixed to MAPbI<sub>2.55</sub>Br<sub>0.45</sub>.

## SI References

1. Sangwan, V. K.; Lee, H. S.; Bergeron, H.; Balla, I.; Beck, M. E.; Chen, K. S.; Hersam, M. C., Multi-Terminal Memtransistors from Polycrystalline Monolayer Molybdenum Disulfide. *Nature* **2018**, 554 (7693), 500-504.
2. Kim, G. Y.; Senocrate, A.; Yang, T. Y.; Gregori, G.; Gratzel, M.; Maier, J., Large Tunable Photoeffect on Ion Conduction in Halide Perovskites and Implications for Photodecomposition. *Nat Mater* **2018**, 17 (5), 445-449.